



TECHNISCHE UNIVERSITÄT WIEN
TECHNICAL UNIVERSITY OF VIENNA

Masterarbeit aus Materialwissenschaften

Photocurrent Measurements on InAs Quantum Dots

ausgeführt am Institut für Festkörperelektronik
der Technischen Universität Wien

Unter Anleitung von:
Univ. Ass. Dr. Wolfgang Brezna
Prof. Dr. Jürgen Smoliner

Vorgelegt von Monika Madl
Gärtnergasse 22, 2320 Kledering

Wien, 12. Mai 2009

Abstract

In this work, the performance of a broadband laser light source in comparison to a halogen lamp for spatially resolved photocurrent spectroscopy studies in the wavelength range of 870-1250nm was evaluated. Measurements were performed using a monochromator and an atomic force microscope (AFM) with an electrically conducting tip on a self-assembled InAs/GaAs quantum dot test sample. The sample structure corresponds to a Schottky-i-n diode, the single dot layer was embedded within the intrinsic region of the sample. The application of an AFM tip as a top electrode allows to determine the photocurrent with sub-micrometer (typically 50nm or better) spatial accuracy, which allows to selectively measure the photocurrent response of individual quantum dots and the single layer InAs quantum well. All spectra show a transition that can be attributed to interband excitation of the wetting layer. Signal intensities, spectral and spatial resolution, pressure and bias dependent behaviour were investigated. Results for the wetting layer were compared to photoluminescence measurements and good agreement between the photocurrent results and the photoluminescence spectra was found.

Contents

1	Introduction	1
2	Theory	5
2.1	Semiconductor properties	5
2.1.1	GaAs and InAs as III-V Semiconductors	5
2.1.2	Semiconductor heterojunctions	8
2.1.3	Effect of restricted dimensions	11
2.2	Photocurrent generation in semiconductors	12
2.2.1	Optical excitation	13
2.2.2	Monochromator basics	15
2.2.3	Photocurrent due to excess charge carriers	17
2.3	Transport of charge carriers	19
2.3.1	Basic equations of semiconductor physics	19
2.3.2	Tunneling	20
2.4	Physics of the tip-sample contact	22
2.4.1	Schottky contact	22
2.4.2	MIS structure and other contacts	28
2.4.3	Charge carrier collection by the AFM tip	30
2.5	Dependence of PC on experimental parameters	32
2.5.1	Wavelength and intensity of incident light	32
2.5.2	Doping and surface states	33
2.5.3	Voltage	34
2.5.4	Pressure	35
2.5.5	Temperature	36

3	Experimental Considerations	37
3.1	Samples	37
3.2	CAFM and its use for PC measurements	38
3.3	Setup for PC measurements	39
3.3.1	Lightsource 1	42
3.3.2	Lightsource 2	47
3.4	Characteristic behaviour of PC spectra	53
3.4.1	Wavelength resolution	53
3.4.2	Pressure dependent behaviour	54
3.4.3	Voltage dependent behaviour	55
3.4.4	Test for spatial resolution	56
3.4.5	Signal stability	58
4	Results	60
4.1	Quantum Dot Spectra	60
4.2	Splitting of the WL signal	61
4.3	FIB effects	64
4.4	Effect of tunnel oxide on PC	67
4.5	Comparison of PC-AFM and device PC spectra	70
4.6	Comparison of PC and PL results	71
5	Conclusion and Outlook	73
6	Project Plan	80

Chapter 1

Introduction

Photocurrent (PC) spectroscopy is frequently applied to study electronic transitions between conduction- and valence band subbands in semiconductor superlattices and structures of reduced dimensionality. It can provide comparable and complementary info to the commonly used purely optical methods such as photoluminescence (PL) or optical absorption spectroscopy. The reason why it is widely used to characterize individual structures with reduced dimensionality is the high accuracy and sensitivity of the method compared to absorption spectroscopy, which becomes difficult for nanostructures, where the fraction of light absorbed is very small [1, 2]. On the other hand, electric currents can be measured down to the fA regime and light sources of very high power are available, which makes PC spectroscopy a very suitable method to obtain information about the electronic structure of such samples.

The idea behind PC spectroscopy is the extraction of photoexcited carriers from the sample by means of an electric field. This occurs under the condition that the transition time to the contacts is smaller than the average carrier lifetime. For quantum dots (QDs)¹ and quantum wells (Qwell) in particular, a PC signal can be observed provided that the tunneling time of photoexcited carriers out of the potential well is smaller than their radiative lifetime. In case that all photogenerated carriers contribute to the PC signal,

¹Quantum dots are small pyramidal structures appearing during epitaxial deposition of strained heterostructures, with a zero dimensional density of states.

the signal intensity is directly related to the absorption strength of the sample [2]. Therefore, PC spectroscopy is regarded as a variation of absorption spectroscopy.² It is a complementary method to photoluminescence spectroscopy which does not reproduce absorption spectra directly but reflects a structure based on intradot relaxation features and LO phonon coupling [3]. In addition, PC spectroscopy also allows to gain information about optically forbidden transitions and can be used for the detailed study of high lying energy states, which is not possible by other methods, such as PL or electroluminescence (EL) spectroscopy to the same extent [4].

PC spectroscopy on p-i-n quantum well photodiodes was done e.g. by Collins in 1986 [5]. Many studies on the interband and intraband optoelectronic properties of p-i-n quantum well and dot devices followed [2, 1, 6]. The features of the spectrum appear at an energy corresponding to intra- inter- or inter- and intrasubband transitions between hole and electron levels, and the intensity is proportional to the occupancy of states and the transition probability. PC spectroscopy is applied to investigate transitions in heterostructures and QD systems, organic films, dielectric materials, NPs, etc. Attempts for spatially localised measurements have been made using shadow masks [7], or scanning probe methods like scanning near field optical microscopy [8] and conducting atomic force microscopy (AFM) measurements [9, 10].

The AFM was originally developed to map the topography of insulator surfaces based on Van der Waals interaction between a flexible tip and the sample. [11]. As the tip is scanned over the surface, the surface topography can be reconstructed from the deflection signal on the nm-level. The principle of mapping interaction forces can be extended to probe chemical, magnetic as well as electric properties by choice of appropriate cantilevers, and several scanning probe techniques were developed for all these applications. The challenge in scanning probe microscopy (SPM) applications is the quantitative analysis of acquired signal. Factors like geometry of the tip-surface system and various contributing interactions complicate matters, but calibration is possible in many cases and then SPM is a quantitative probe

²The relation is given by $I = APe/hf$, where P is the intensity and f the frequency of light incident on the sample, A the strength of absorption and I the photocurrent [2].

of local physical properties on the nanoscale.

Conducting AFM (CAFM), also called conducting probe AFM, or scanning spreading resistance microscopy, allows for two basic kinds of measurements: stationary point contact recording of I-V curves and 2-dimensional current/resistance maps at fixed voltages. For PC measurements, the electrically conducting tip is used as the top electrode and can be positioned anywhere on the sample surface. Measuring the photogenerated current with an AFM tip is a relatively new idea.[9] Hereby, one can make use of the detailed spatial resolution of the AFM (under ambient conditions down to 10-20nm) and obtain information about the spatial distribution of photocurrent generated on inhomogeneous materials, e.g. organic electronic devices [12], QDs and quantum wires [13, 6], etc. These studies are extremely useful to enhance our understanding of the current generation, transport and loss in small structures and at structure boundaries.

Recent interest in self-assembled QDs was fuelled by their application potential in optoelectronic devices such as ultralow threshold QD lasers [14] and QD infrared photodetectors [15]. For these applications, InAs/GaAs³ quantum dot systems are under intense investigation. Due to their small size, quantum dots possess discrete, zero dimensional electronic states. Controlling single excitonic QD states by electronic or optical means allows to create applications such as single photon sources and basic devices for quantum information processing. [16] Knowledge of the energy spectrum of QDs is important to tune and describe lasing and related information about the spectral position of excited states can be gained by spectroscopy. One very suitable technique to study QD transitions is PC spectroscopy, sensitively detecting electronic transitions. Furthermore, PC spectroscopy performed using a conducting AFM tip can also probe single quantum dots and yield spectra free of ensemble related broadening.⁴

To sum up, by measuring the photocurrent of semiconductors, information about the band structure and the density of states can be obtained. For the special case of one-dimensional semiconductors, like quantum dots,

³indium arsenide/gallium arsenide

⁴Self-assembled quantum dots grow on the same sample generally have a size distribution of around 20%, which results in broadening of the signal peaks for ensemble spectra.

the density of states is made up of several sharp lines, delta functions, that also appear in photoemission, -absorption and photocurrent spectra and are directly related to the energy levels of the dots. However, in order to measure the spectrum of a quantum dot, the dot needs to be separated from the ensemble, from the other dots on the sample. This is usually achieved by fabricating some kind of mesa structure, that only exposes regions with very few quantum dots for measurement. Many of these measurements are done at low temperatures to eliminate thermal effects. CAFM has the big advantage to allow localised photocurrent measurements at room temperature, showing discrete lines that can be related to electronic transitions. This work on photocurrent AFM (PC-AFM) spectroscopy compares the performance of a broadband laser light source to a halogen lamp for spatially resolved photocurrent spectroscopy studies by means of a conducting AFM. Measurements were performed using a monochromator and an AFM with an electrically conducting tip on a self-assembled InAs/GaAs QD test sample.

The following chapters are organised as follows: In the second chapter, basic semiconductor theory necessary for the understanding of photocurrent generation and transport is presented. This includes information about the band structure of GaAs and InAs, photoexcitation, current transport and physics of the tip-sample contact and the effect of certain parameters on the band structure of the InAs/GaAs heterostructure. The third chapter describes our measurement setup and the change in performance by implementing the broadband laser. Experimental evidence for the dependence of the PC response on factors like applied bias and tip pressure is investigated along with the spatial and spectral resolution of the method. Finally the results are presented, on QDs, detailed study of the wetting layer signal also in comparison with PL data, defect level PC and PL and effects of surface preparation and contamination are shown.

Chapter 2

Theory

This chapter presents the theoretical background required to understand the principle behind photocurrent measurements and the basic electrical properties of our sample materials. The chapter is structured in five sections. In the first section, properties of the InAs/GaAs quantum dot samples are explained, the second section deals with the mechanism of photocurrent generation in semiconductors, the third section explains the transport of charge carriers to the contact, the fourth section explains particularities of the tip-sample contact and in the last section the dependence of the photocurrent on various experimental parameters is discussed.

2.1 Semiconductor properties

2.1.1 GaAs and InAs as III-V Semiconductors

GaAs and InAs are both binary III-V semiconductors with a zincblende structure of interpenetrating fcc lattices, one containing the atom of group III (Ga, In), the other made up of atoms of group V (As). The zincblende crystal structure along with the calculated electronic band structure for both compounds is shown in Fig. 2.1.

These energy bands result from the interaction between atoms in a periodic lattice with two different interatomic distances. For a semiconductor, the energy bands can be grouped into the valence band (VB) and the conduction band (CB), with a bandgap of magnitude E_g in between as illustrated

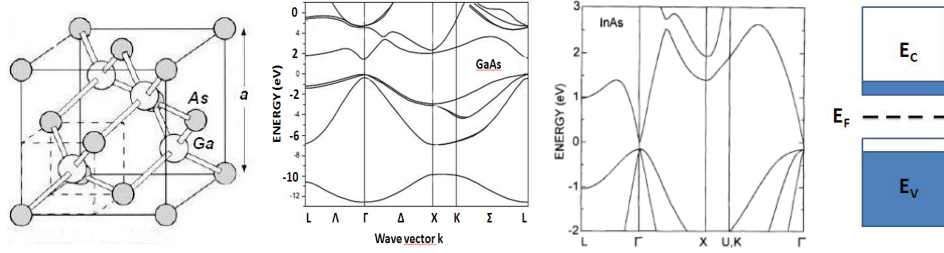


Figure 2.1: Zincblende crystal lattice, band structures for GaAs and InAs, and schematic band structure of a semiconductor. Lattice and band structures adapted from [17].

in Fig. 2.1. The bandgap is the minimum distance between valence and conduction bands. For GaAs, the minima of the CB is above the maxima of the VB, so GaAs is a direct bandgap semiconductor.

The most important material parameters of InAs and GaAs with respect to optoelectronic applications are listed in Table 2.2. There is an obvious difference in the lattice constants of InAs and GaAs, and this lattice mismatch results in a strained island, also called Stranski-Krastanow growth [18, 19] of InAs when grown epitaxially on GaAs. For a thin layer of InAs, this leads to formation of pyramids on the nanometer scale.

Symbol	Description	Value	Unit
ϵ_{GaAs}	Relative permittivity of GaAs	13.18	
$m_{\text{eff,GaAs}}$	Effective mass of electrons in GaAs	0.063	m_0
$E_{\text{g,GaAs}}$	GaAs band gap energy (at 300K)	1.424	eV
a_{GaAs}	Lattice constant of GaAs	5.65325	\AA
ϵ_{InAs}	Relative permittivity of InAs	15.15	
$m_{\text{eff,InAs}}$	Effective mass of electrons in InAs	0.0239	m_0
$E_{\text{g,InAs}}$	InAs band gap energy (at 300K)	0.354	eV
a_{InAs}	Lattice constant of InAs	6.0583	\AA

Table 2.1: Material parameters for GaAs and InAs

At $T=0\text{K}$ the VB of a semiconductor is fully filled, there are no states for charge carriers and no current can flow. When energy is supplied to the semiconductor in form of heat, electromagnetic radiation or external



Figure 2.2: Schematics of the Stranski-Krastanow growth mode.

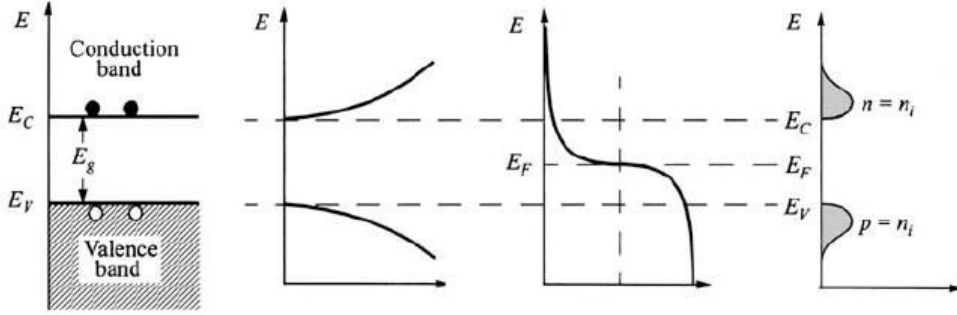


Figure 2.3: Band diagram, density of states, FD-distribution and charge carrier concentrations for an intrinsic semiconductor

contacts, electrons can be lifted into the states of the conduction band leaving hole states behind in the valence band. The number of mobile charge carriers increases until the system reaches the new equilibrium state.

The concentration of mobile charge carriers, n for electrons, p for holes, is given by

$$n = \int_{E_C}^{\infty} f(E) N(E) dE \quad (2.1)$$

$$p = \int_{-\infty}^{E_V} 1 - f(E) N(E) dE \quad (2.2)$$

where $N(E)$ is the density of states and $f(E)$ gives the occupancy of the state. The occupancy is described by Fermi-Dirac (FD) statistics, where E_F is the Fermi energy.

$$f_{\text{FD}}(E) = \frac{1}{1 + \exp \frac{E - E_F}{kT}}.$$

Fig. 2.3 shows the schematic band diagram, density of states, FD-distribution and charge carrier concentrations for an intrinsic semiconductor. The electron density and thus the electronic properties of semiconductors can be easily tuned by doping the material, that is substituting some atoms in

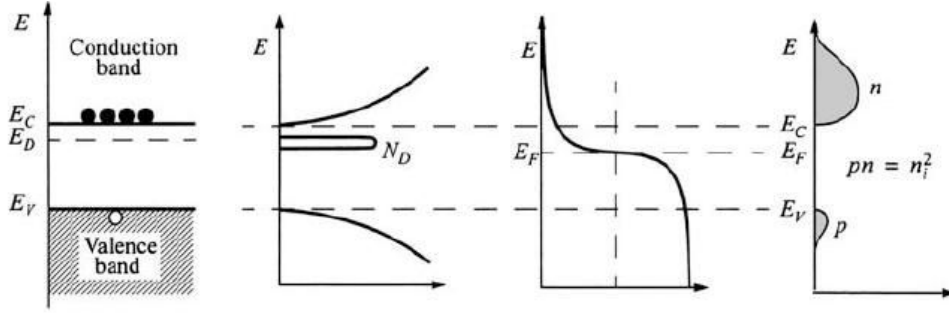


Figure 2.4: Band diagram, density of states, FD-distribution and charge carrier concentrations for an n-type semiconductor

the crystal for atoms with different valence states. Substituent atoms with less valence electrons than the original atom are called acceptors, with more electrons are donors. A semiconductor doped with acceptors is p-type, since there are more positive hole states than in the intrinsic case, doping with electron donors results in higher electron densities and an n-type material. Our samples are made up of intrinsic and n-type layers. Fig. 2.4 shows the schematic band diagram, density of states, FD-distribution and charge carrier concentrations for an n-type semiconductor.

2.1.2 Semiconductor heterojunctions

A heterojunction is a junction between two dissimilar semiconductors, which also means different energy gaps, in contact and is used for various device applications. For devices, matching of the lattice constants is an important design parameter in order to have a good quality interface between the layers of different materials, otherwise interface traps are present causing electric defects. The choice for heterojunction materials are semiconductors with different energy gaps but similar lattice constants. For thin layers, a certain degree of lattice mismatch can be deposited free of defects forming a strained layer. The critical thickness t_c of the strained layer, where too much strain has built up and transition to the relaxed state results, is given by an empirical formula according to [17]:

$$t_c \approx \frac{a_e^2}{2|a_e - a_s|} \quad (2.3)$$

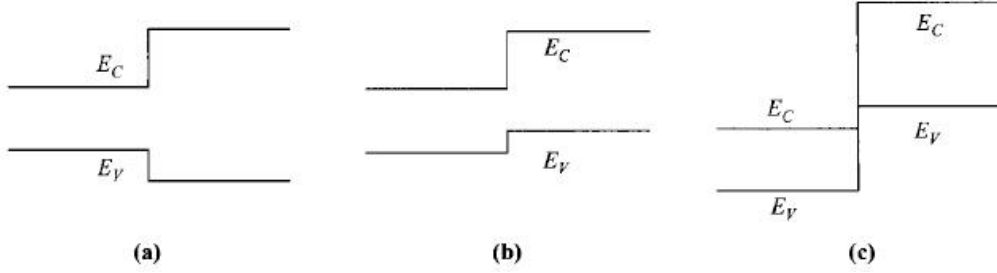


Figure 2.5: Different types of heterojunctions: straddling (a), staggered (b) and broken-gap type (c). [17]

where a_e and a_s are the respective lattice constants of the epitaxial layer and the substrate. For 5% lattice mismatch and a lattice constant around 5\AA , t_c is about 10nm. In case of InAs on GaAs, where the lattice mismatch is about 7 percent, the critical thickness calculated according to (2.3) gives 4.5nm. In practice, the transition from a layered growth to an island-like growth mode already occurs at a thickness of 1-4 monolayers, corresponding to 0.5-3nm, depending on the concentration of In on the surface of GaAs. [18] In general, not only are the energy gaps different, but also the electron affinities, resulting in different alignments of the conduction and valence bands at the interface. According to the band alignment, there are 3 types of heterojunctions to distinguish, as shown in Fig. 2.6. In Type I or straddling heterojunctions one material has both lower E_v and higher E_c , where E_v and E_c are the energies of the upper edge of the CB and the lower edge of the VB respectively. In type II or staggered junctions, one material has both higher E_v and E_c and in type III or broken gap heterojunctions, which is a subtype of type II, the E_v of one material overlaps with the E_c of the other at the interface. A GaAs/InAs heterojunction belongs to type I, for InAs grown on GaAs substrate.

Due to the difference in the energy gap between the CB and the VB, when a thin InAs is sandwiched between GaAs layers, a quantum well forms as shown in Fig. 2.6 a). When depositing about one monolayer of InAs on GaAs, the layer is strained due to the lattice mismatch between InAs and GaAs. InAs has a larger lattice constant than GaAs and as a consequence, island-like growth mode occurs for the 1st layer of InAs. Thus, in general,

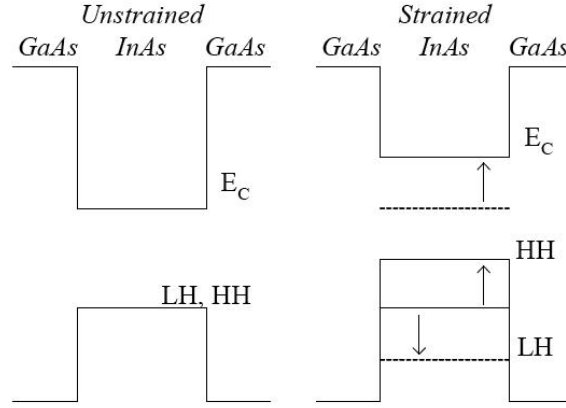


Figure 2.6: Energy levels of an unstrained and a strained heterojunction of InAs and GaAs.

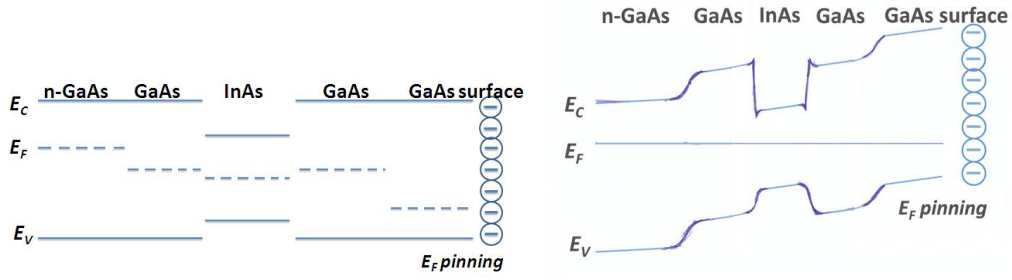


Figure 2.7: a) Relative energy levels in the unconnected semiconductors. b) Schematic band structure after alignment of the Fermi levels.

there is a thin layer InAs on the surface - a quantum well in the band diagram - that "buckles" in places forming 3-dimensional structures on the nm-scale, so called quantum dots and the frequency of the buckling depends on the growth conditions.

When two such different semiconductors are brought into contact, the Fermi levels have to align, resulting in a band bending as illustrated for the structure of our sample in Fig. 2.7. The additional band bending at the left side of the diagram is a result of the surface state pinning of the Fermi level, which is a result of the large number of surface defects present on the semiconductor surface. The surface defects manifest themselves as a defect band located in the energy gap of the semiconductor at approximately $E_g/3$

above the upper edge of the valence band. $E_g = E_c - E_v$ is the bandgap energy. Depending on the location of the Fermi level E_F relative to the defect band, the defect states can be occupied or empty. Any change in the Fermi level results in a change in the occupancy of the defect levels and a change in the surface charge on the semiconductor, which is energetically unfavourable. Thus the Fermi level is pinned within the defect band at the surface, and lies at $E_F = E_v + 1/3E_g$.

2.1.3 Effect of restricted dimensions

The differences in energy between the conduction and valence bands can be used to form barriers for carriers. A quantum well for holes or electrons is formed if in a three layer material the middle layer has the higher E_v or the lower E_c respectively. Thus, a quantum well introduces a confinement along one spatial direction and confines charge carriers to 2D system, The energy states within the well are no longer continuous but quantized. The most-important parameters for a quantum well are the well width L , and well height. The confining potential is obtained from the conduction-band and valence-band offsets. Since the potential is not infinite, the wavefunction in the confined region leaks out of the well with a finite probability. If an electric field is applied to the system, there is a tilting of levels corresponding to the applied field, which allows for tunneling of carriers through a triangular barrier. The minimum requirements for forming a quantum well of length L_x are that the quantised energy $\frac{\hbar^2 \pi^2}{2m_{\text{eff}} L_x^2} \gg k_B T$ where $k_B T$ is the thermal energy and m_{eff} the effective mass of electrons or holes. L_x needs to be smaller than the mean free path and the de Broigle wavelength. Inside the well the conduction band is divided into subbands and carriers reside in these subbands only, so that the effective energy gap for interband transitions is larger in a quantum well than in the pure bulk semiconductor.

Reducing the physical dimensions of semiconductors to the order of the de Broigle wavelength has a significant impact on their electronic properties. If the confinement of carriers is also extended to other directions, 1D (quantum wires) and 0D (quantum dots) systems can be created. Depending on the degree of confinement, the density of states $N(E)$ has different shapes as

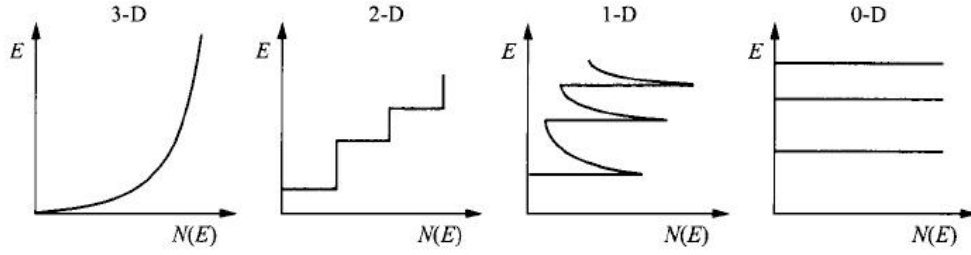


Figure 2.8: Density of states for different dimensionalities.

function of the energy, as shown in Fig. 2.8. The density of states (DOS) is important for semiconductor systems, because the carrier concentrations and their distribution in energy is given by equation 2.1, which is just the DOS multiplied by a Fermi-Dirac distribution. For a 3D system, $N(E) \propto \sqrt{E}$, for a 2D system it has a form of a step function, a 1D system has an inverse energy relationship $N(E) \propto 1/\sqrt{E}$ and the DOS of a 0D system is delta function like. The DOS of a material plays an important role in photoexcitation and is reflected in a photocurrent spectrum. Therefore, when using excitation energies lower than the bandgap of GaAs, one can expect a broad peak to appear for the QWell, and several sharp, broadened delta-function like peaks for the QDots.

2.2 Photocurrent generation in semiconductors

Optical measurements are very important for determining the band structure of semiconductors. Photon induced electronic transitions can occur between different energy bands giving information about the band energy. This section explains optical theories, such as excitation and photocurrent generation in semiconductors as well as optical principles for the operation of a monochromator.

2.2.1 Optical excitation

When energy is supplied to the electrons in a semiconductor in form of radiation, two different types of transitions are possible depending on the energy of the incoming light. For $E_{\text{photon}} = hf > E_g$ interband transitions are dominant, these are electronic transitions between valence and conduction bands. At lower energies, intraband transitions occur, these are transitions between the energy levels of the same band. An additional possibility of transitions arises from defect levels in the bandgap that can also host electrons. Defect levels in semiconductors can often be approximated by the energy levels of the hydrogen atom¹, which works reasonably well for shallow defects in semiconductors with a zincblende structure, like GaAs. Thus, defect levels can appear as distinct lines in the absorption or emission spectrum. Interband transitions are of interest, because as an electron is lifted into the CB leaving a hole behind in the VB, the number of available carriers in the semiconductor temporarily increases. Energy and momentum are conserved in the photon-electron interaction, where the momentum of the photon is negligible compared to the momentum of the electron and phonons are important mediators of energy and momentum in indirect semiconductors.

In direct bandgap materials, allowed transitions for electrons are between states with the same wavevector. The photon energy is approximately equal to (or larger than) the bandgap energy of the direct semiconductor. For indirect bandgap materials, momentum conservation is only possible through assistance of a phonon, such transitions are called indirect transitions. For direct semiconductors, the minima of the conduction band lies vertically above the maxima of the valence band. Optical transitions can be represented in an $E(k)$ -diagram as vertical lines, which means that $\Delta k = 0$, where $\vec{k} = \frac{2\pi}{\lambda}$ is the wavevector. The transition probability between an empty state in the CB (E_2) and a filled state in the VB (E_1) is determined by Fermi's Golden

¹Energy levels of a hydrogen atom: $E_n = -\frac{m_{\text{eff}}e^4}{32(\hbar\varepsilon\pi)^2} \frac{1}{n^2}$, where $n = 1, 2, 3, \dots$

Rule.² The energy relation assuming parabolic band profiles is

$$E_2 - E_1 = \frac{\hbar^2 k^2}{2m_{\text{eff,p}}} + E_g + \frac{\hbar^2 k^2}{2m_{\text{eff,n}}} = \hbar\omega \quad (2.4)$$

where $\omega = 2\pi f$.

The absorption coefficient $\alpha(E_{\text{photon}})$ is determined by the density and occupancy of states in the CB and the VB and shows a frequency dependency.

$$\alpha(\omega) = \sigma(\omega)N_j(\omega)(f_{\text{abs}} - f_{\text{em}}) = \sigma(\omega)N_j(\omega)(f_v(E_1) - f_c(E_2)) \quad (2.5)$$

The combined density of states, that gives the density of pairs of states that can participate in a transition in the interval $\omega \rightarrow d\omega$ is

$$N_j(\omega) = \frac{(2mr)^{3/2}}{2\pi^2\hbar^2} \sqrt{\omega - E_g} \quad (2.6)$$

The occupancy of the bands is accounted for by the Fermi-Dirac function³, f_c and f_v for the conduction and valence bands respectively. The transition rate is given by $f_{\text{abs}} - f_{\text{em}} = f_v(E_1) - f_c(E_2)$.

At low temperatures and low intensities, the absorption coefficient for parabolic bands results as

$$\alpha_0(\omega) = \sigma \sqrt{\hbar\omega - E_g} \quad (2.7)$$

Close to the absorption edge, excitonic interactions play an important role, resulting in deviations from the above described behaviour. Excitons are electron hole pairs bound together by the Coulomb interaction, with a binding energy corresponding to the energy of the hydrogen atom, E_n , where the mass is replaced by the reduced mass of the electron-hole complex. Thus, excitonic transitions at the absorption edge can occur at $E_{\text{ex}} = E_g - E_n$. Generally, only the first order excitonic transition is observed, leading to an enhanced absorption coefficient just below the absorption edge.

²Fermi's Golden Rule says that the transition probability T is given by $T_i f = \frac{2\pi}{\hbar} |\langle \phi_i | c + |\phi_f \rangle|^2 N(E_f - E_i - \hbar\omega)$, where i denotes the initial state and f the final state, ϕ is the electron wavefunction and E its energy.

³Fermi-Dirac function: $f(E) = \frac{1}{1 + \exp \frac{E - E_F}{kT}}$

2.2.2 Monochromator basics

Illumination with distinct wavelengths is a prerequisite in order to obtain a photocurrent spectrum of the semiconductor sample. To split the polychromatic light coming from a conventional light source, monochromators are frequently used. The working principle of the monochromator is sketched in Fig. 2.9. Incoming light is collimated and reflected onto a diffraction grating. A second mirror refocuses the dispersed light onto the exit slit. Each colour arrives at a separate point in the exit slit plane and the range of colours leaving the exit slit is determined by the slit width. By rotation of the diffraction grating, the band of colours moves relative to the plane of the exit slit. The desired wavelength leaves the monochromator through the exit slit. Plane grating monochromators have an exit slit through which a narrow spectral region passes and the center wavelength of this spectral region is changed by rotating the grating. The grating equation for the selected wavelength under the condition that incident and diffracted rays lie in a plane perpendicular to the grating, is given by

$$m\lambda = d(\sin \alpha + \sin \beta) = 2d \sin \gamma_b \quad (2.8)$$

where γ_b is the facet angle and $m = 1, 2, 3, \dots$ is the spectral order. The right side of the equation represents the path difference between waves from adjacent grooves as shown on Fig. 2.10. Constructive interference occurs when this path difference is a integer multiple of the wavelength λ . Multiple order diffraction behaviour has the disadvantage that successive spectra overlap.

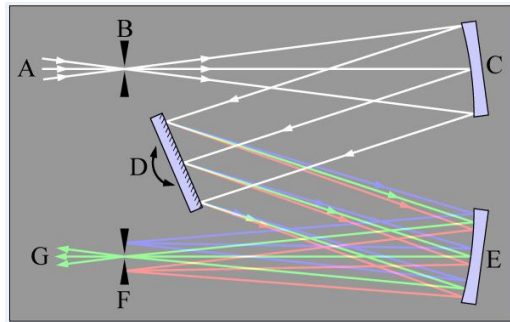


Figure 2.9: Light path and color dispersion in a Czerny-Turner monochromator.[20]

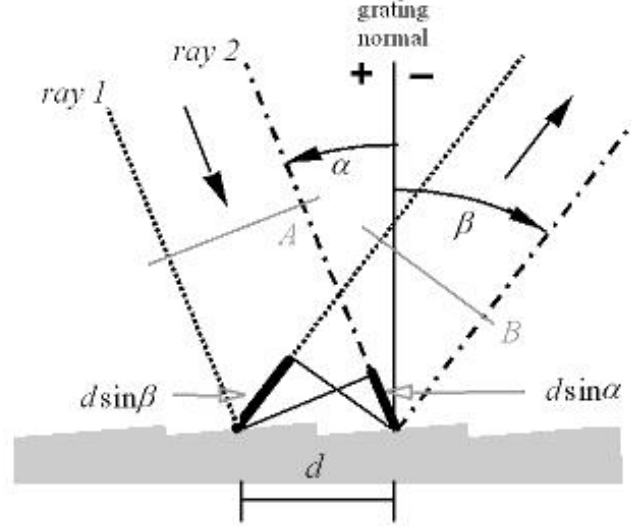


Figure 2.10: Path difference for two rays diffracted from adjacent grooves. Adapted from [21].

So for any grating configuration, the light of wavelength λ diffracted in the first order $m = 1$ will coincide with the light of wavelength λ/n diffracted in the n^{th} order with $m = n$. Using filters that cut out wavelength of higher spectral orders prevents this superposition of wavelengths, which would lead to ambiguous data. The resolving power of the grating, $R = \frac{\lambda}{\Delta\lambda}$ represents its ability to separate adjacent spectral lines of wavelength α , where $\Delta\lambda$ is the limit of resolution, the smallest difference in wavelength that can be distinguished. The resolving power of a planar diffraction grating is given by

$$R = mN = \frac{Nd(\sin \alpha + \sin \beta)}{\lambda}, \quad (2.9)$$

where m is the diffraction order and N the number of grooves illuminated on the grating. The maximum resolving power for a planar grating with uniformly distributed groove spacing d is $R_{\text{max}} = 2W/\lambda$, where W is the rule width of the grating. This maximum resolving power is achieved at grazing incidence. An important parameter of the grating is the angular or spatial dispersion, which is a measure of angular or spatial separation between diffracted light of different wavelength. Angular dispersion D_{alpha} expresses the spectral range per unit angle and can be obtained by differentiating the

grating equation, assuming constant angle of incidence α .

$$D_{\alpha} = \frac{\partial \beta}{\partial \lambda} = \frac{m}{d \cos \beta} \quad (2.10)$$

The angular dispersion increases with the groove frequency, $G = 1/d$. The linear dispersion is the product of the angular dispersion D and the effective focal length $f'(\beta)$ of the system. The reciprocal linear dispersion $[P] = \text{nm/mm}$ is a measure of the change in the wavelength corresponding to the change in location along the spectrum. P is just given by

$$P = \frac{d \cos \beta}{m f'} \quad (2.11)$$

The spectral bandpass $B \geq w'P$ is the wavelength range that passes through the exit slit and is often defined as the difference in wavelength at half maximum intensity, where w' is the width of the exit slit in nm. Bandpass can be reduced to a certain limit by decreasing the exit slit at the cost of light intensity.

2.2.3 Photocurrent due to excess charge carriers

In general, when light is shone on a thin n-type semiconductor, with thickness smaller than one over the decay length of radiation in the material, electron-hole pairs are generated uniformly throughout the sample with a generation rate G_p , an excess of charge carriers compared to the initial state is built up. When the light is switched off, there is no more generation and the system relaxes back to the initial state through recombination.

The wavelength requirement for carrier generation is $\frac{hc}{\lambda} \geq E_g$, that is, the energy of the incident photons has to be larger than the bandgap of the semiconductor. Band-to-band recombination and excitation does not correspond exactly to the bandgap, because due to the thermal energy, the electrons and holes reside slightly above and below the respective band edges. For a quantum well, the electron profile at the band edge is much sharper than in a 3D case, due to the constant DOS within each subband. If the thickness of the sample is large, the illumination intensity decays according to $e^{-\alpha x}$, where $\alpha \approx 10^6 \text{cm}^{-1}$ is the absorption coefficient, and consequently

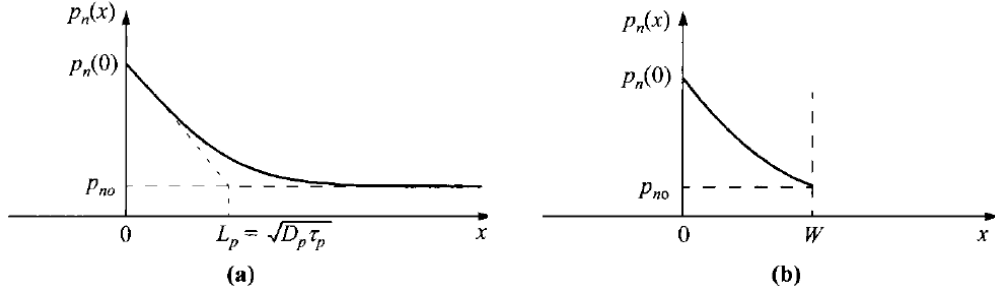


Figure 2.11: Excess charge concentration as function of distance from the surface, a) in a very long sample b) in a sample of length W . [17]

a decay in carrier concentration with the distance from the illuminated face is also observed. Considering only the direction away from the surface, the charge density $p(x)$ can be found by solving

$$\frac{dp_n}{dx} = \frac{-p_n - p_o}{\tau_p} + D_p \frac{d^2 p_n}{dx^2} \quad (2.12)$$

which can be derived from the one-dimensional continuity equation 2.19. The solution is given by

$$p_n(x, t) = p_o + \frac{N'}{\sqrt{4\pi D_p t}} \exp -\frac{x^2}{4D_p t} - \frac{t}{\tau_p} \quad (2.13)$$

for the zero field case, where N is the number of electrons or holes generated initially per unit area. If an electric field is present along the sample, x in the solution is replaced by $x - \mu_p \vec{E}t$, where \vec{E} is the electric field. This will expand or reduce the width of the distribution, depending on the relative direction of electric field and charge carrier movement due to the concentration gradient. Fig. 2.11 shows the concentration gradients that result in a thick sample and a sample of thickness W , that is smaller than the diffusion length of charge carriers, $L_p = \sqrt{D_p \tau_p}$.

In GaAs, the values for the diffusion length are in the order of 10^{-2} cm, in Si up to one cm. As the charge carriers diffuse away from the point of injection, some also recombine, accelerating the decay of the charge carrier density. When an InAs quantum well sandwiched between GaAs layers is illuminated with light with wavelength above the GaAs bandgap, excitation

of charge carriers only occurs in the InAs quantum well, since GaAs is transparent to light in the wavelength range $\lambda > \frac{hc}{E_g}$.

Additionally, some excitation across the Schottky barrier, with barrier height ϕ_B ⁴ at the surface might occur, since the condition for internal photoemission of a metal-semiconductor contact, $e\phi_B < hf < E_g$ is fulfilled for GaAs in the range 870-1350nm. Assuming that the main mechanism of carrier generation is excitation across the InAs layer, one can say that the excess carriers in the InAs quantum well can escape by tunneling, electrons moving towards the back contact and holes towards the surface, guided by the built-in electric field.

As the diffusion length for carriers in GaAs is in the order of 100 μ m but both back and front contacts are closer to the InAs layer than that, the charge carrier distribution is mainly determined by the distance to the contact. Towards the back surface, carriers are extracted at the highly n-doped conductive GaAs:Si layer, so that $W=40$ nm. Towards the illuminated front surface, carriers travel $W=120$ nm before they are extracted. Over these distances, it can be assumed that the excess charge carrier density stays essentially the same as at the point of carrier injection. The built in potential acts as an electric field, accelerating the holes towards the front surface and the electrons towards the back surface.

2.3 Transport of charge carriers

2.3.1 Basic equations of semiconductor physics

The behaviour of charge carriers in semiconductors under the influence of electric fields and/or optical excitations can be described by electrostatic, current density and continuity equations. For electrostatics, one of the most important equations is Poisson's equation:

$$\nabla^2 \phi = -\frac{\rho(x, y, z)}{\epsilon} \quad (2.14)$$

where ϕ is the electric potential and ρ the charge density. Poisson's equation gives the potential and for a given charge distribution ρ . The movement

⁴The Schottky barrier will be explained in detail in section 2.3

of charge carriers due to concentration gradients (diffusion component) and applied electric fields (drift component) is described by the current density equations under steady state conditions.

$$J_n = en\mu_n E - eD_n \frac{dn}{dx} \quad (2.15)$$

$$J_p = ep\mu_p E - eD_p \frac{dp}{dx} \quad (2.16)$$

$$J_t = J_n + J_p \quad (2.17)$$

Here, J_{cond} is the total current density composed of electron and hole current density. μ_n and μ_p give the mobility of electrons and holes respectively, $D_n = \frac{kT}{e}\mu_n$ and $D_p = \frac{kT}{e}\mu_p$ are the diffusion constants and dn and dp are the concentration gradient of charge carriers. The effects from external magnetic fields (magneto-resistive effects) are not considered here. Continuity equations deal with the time dependent change in carrier concentration, such as carrier injection, generation and recombination.

$$\frac{dn}{dt} = G_n - U_n + \frac{1}{e}\nabla J_n \quad (2.18)$$

$$\frac{dp}{dt} = G_p - U_p + \frac{1}{e}\nabla J_p \quad (2.19)$$

G_n and G_p are the respective electron and hole recombination rates, U_n and U_p are the effective recombination rates and can be expressed as $U_n = \delta n / \tau_n$. Excess carriers can be generated in a semiconductor by impact ionisation under high electric fields or optical excitation with photons of the right energy. Injection from a nearby contact is also a possibility. For our application, carrier generation by means of optical excitation is the most important mechanism.

2.3.2 Tunneling

Tunneling is a quantum-mechanical phenomenon that allows a charge carrier with energy smaller than the barrier height to pass through the barrier. This can be explained by the wave nature of the particle, there is some finite probability for the particle to exist inside the barrier and it can leak through, if the barrier is thin enough. The transition probability is the amplitude

squared of the wavefunction behind the barrier, and can be found by solving the time-independent one dimensional, single particle Schrödinger equation.

$$-\frac{\hbar^2}{2m} \frac{\partial^2}{\partial x^2} \psi(x) + V(x)\psi(x) = E\psi(x) \quad (2.20)$$

where $V(x)$ is the potential energy, E the energy and $\psi(x)$ the wavefunction of the particle. The solution to the wavefunction is of the general form

$$\phi(x) = A_1 \exp(ikx) + A_2 \exp(-ikx) \text{ for } k = \sqrt{\frac{2mE}{\hbar^2}} \quad (2.21)$$

$$\phi(x) = A_1 \exp(\kappa x) + A_2 \exp(-\kappa x) \text{ for } \kappa = \sqrt{\frac{2m(V-E)}{\hbar^2}} \quad (2.22)$$

The potential for a tunneling barrier is shown in Fig. 2.12, the electron travels as a free electron before and after the barrier and only feels the influence of the potential inside. Matching the solutions at the boundaries, the final solutions

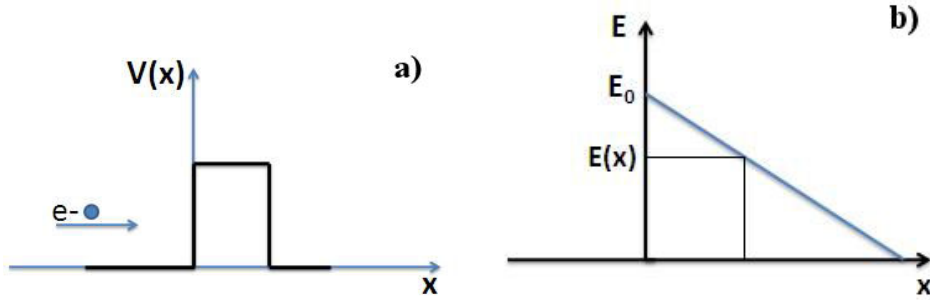


Figure 2.12: Schematics to illustrate the potential for an electron tunneling through a (a) rectangular barrier, b) triangular barrier.

to the problem can be obtained for the one dimensional, one particle case. The amplitude squared for the wavefunction behind the barrier gives the transmission probability for the electron. It can be shown that if $kW \gg 1$, where k is the electron momentum as defined above and W is the width of the barrier, the transition probability for a triangular barrier is given in the WKB (Wentzel-Krammers-Brillouin) approximation by

$$T \approx \exp \left[-2 \int_W^0 |k(x)| dx \right] \quad (2.23)$$

where k is the wave vector of carriers and $W = \frac{E_0}{e\varepsilon}$ is the barrier width at its maximum. The wave vector k can be obtained from the $E - k$ relationship. The barrier height, that is the potential energy, at position x as shown in Fig. 2.12 is $E(x) = E_0 - e\varepsilon x$, where ε is the slope of the barrier and $E_0 = E_{\text{c,GaAs}} - E_{\text{c,InAs}}$. The wave vector inside the barrier is given by

$$k(x) = \sqrt{\frac{2m_{\text{eff}}}{\hbar^2}(E(x) - E)} \quad (2.24)$$

where E is the energy of the particle. For a large tunneling probability, the electric field and the energy of the particle incident on the barrier should be large.

2.4 Physics of the tip-sample contact

For photocurrent measurements it is important to understand the physics of the tip-sample contact, which can be best explained in terms of the Schottky model. The Schottky model describes the rectifying behaviour of semiconductor-metal junctions. Although the tip we are using is not a metal, but Si coated with highly doped diamond, the Schottky model adequately deals with the conduction behaviour of such contacts.

2.4.1 Schottky contact

When a good conductor, typically a metal, is brought into contact with a semiconductor surface, there is a flow of electrons from the semiconductor to the metal or vice versa until an equilibrium is reached and the Fermi levels of the metal and the semiconductor coincide. In an n-type semiconductor, electrons flow to the metal, leaving behind a depletion region in the semiconductor. The field in the depletion region manifest itself as a band bending at the contact as shown in Fig. 2.13, creating an energy barrier, which controls the conduction and capacitance behaviour of the junction. The height of the barrier for electrons flowing from the metal to the semiconductor is ϕ_{Bn} for

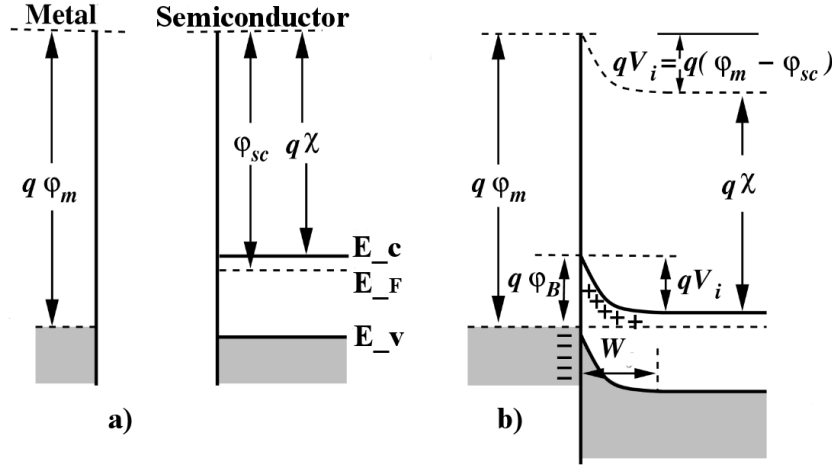


Figure 2.13: Energy band diagram of a metal and an n-type semiconductor first separated (a) then brought into contact (b). Adapted from [22]

n-type and ϕ_{Bp} p-type semiconductors.

$$e\phi_{Bn} = e(\phi_m - \chi) \quad (2.25)$$

$$e\phi_{Bp} = E_g - e(\phi_m - \chi) \quad (2.26)$$

$$e(\phi_{Bn} + \phi_{Bp}) = E_g \quad (2.27)$$

respectively, if the interface itself is assumed to be very thin and transparent to electrons. The band bending corresponds to the built-in-voltage V_b and is given by $V_b = \phi_m - \chi - \phi_n$, where ϕ_m is the work function of the metal, χ the electron affinity of the semiconductor and ϕ_n the distance between E_C and E_F in the semiconductor. The electron affinities of many semiconductors, e.g. GaAs are around 4eV, the work functions of metals are typically between 2-6eV. However, most often the band bending is determined by the presence of surface states of the semiconductor and have only a weak dependence on the metal. The width of the depletion layer W_D in the semiconductor under the approximation that $\rho = eN_D$ for $x < W_D$ and zero otherwise is given by

$$W_D = \sqrt{\frac{2\varepsilon_s}{eN_D}(V_b - V - \frac{kT}{e})} \quad (2.28)$$

Here, ε_s is the dielectric constant of the semiconductor N_D the dopant concentration and V is the externally applied potential. The width of the depletion layer depends on the doping concentration and is generally in the range

of micrometers. Calculating the width of the depletion layer in GaAs for $N_D=10^{18} \text{ cm}^{-3}$ gives a depletion width of about 3.5μm. The electric field in the depletion region $|E(x)|$ and the space charge per unit area Q_{sc} and the depletion layer capacitance per unit area C_D are

$$|E(x)| = \frac{eN_D}{\varepsilon_s}(W_D - x) \quad (2.29)$$

$$Q_{sc} = eN_D W_D \quad (2.30)$$

$$C_D = \frac{\varepsilon_s}{W_D} = -\frac{Q_s}{d\psi_s} \quad (2.31)$$

Such a semiconductor-metal contact is called a Schottky contact and the barrier resulting from band bending is called the Schottky barrier. However, these simple relationships are not observed experimentally, mostly because the values of the work function are strongly affected by the quality of the interface, contamination and the presence of interface states. In general, there is an unavoidable interface layer on the surface with different properties to the bulk, most often oxide creating a potential barrier, as well as interface states due to e.g. reconstruction or dangling bonds at the surface. In addition, image-forces also play a role in determining the transparency of the interface to charge carriers. Thus, the interface properties are the most important in determining the properties of the metal-semiconductor junction. So in reality, the Schottky barrier height is mainly determined by the interface states of the semiconductor and has only a weak dependence on the metal. On GaAs the Schottky barrier height is about 0.9eV and at zero external bias condition the system is in equilibrium, electrons can only overcome the barrier by thermally activation or tunneling. For holes, however, there is no barrier between the semiconductor and the metal so they can freely flow. Nevertheless, this hole diffusion current is very low under normal operating conditions. In order to give a complete picture of the physics at the tip-sample contact, it needs to be mentioned, that there is also a thin oxide layer separating the intrinsic semiconductor region from the metal. To a first approximation, this oxide layer is handled as a very thin barrier, where charge carriers can tunnel through.

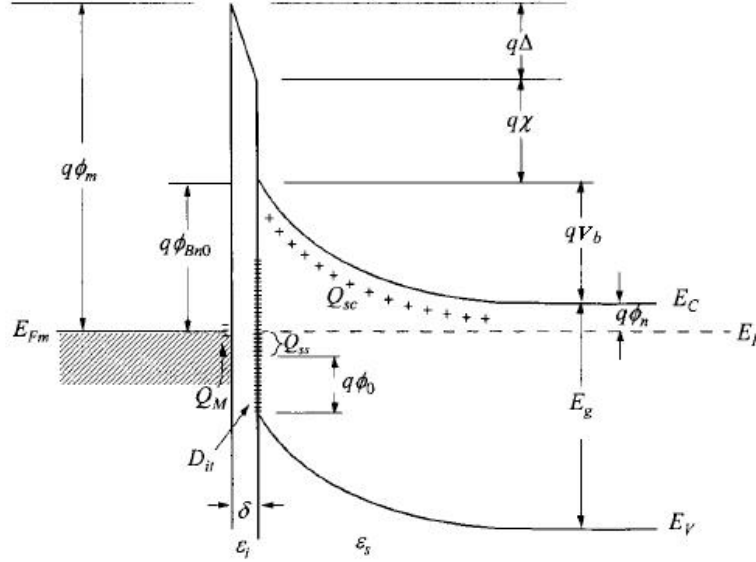


Figure 2.14: Detailed energy diagram of a more realistic metal-n-semiconductor junction, showing the interfacial charge. [17]

A more realistic Schottky model

The barrier height can be estimated based on following assumptions: firstly, there is an interfacial layer of atomic dimensions which is transparent to electrons and but can withstand potential across it, secondly, the number of interface states per unit area per energy is determined by the nature of the semiconductor alone. Fig. 2.14 shows a band diagram of a practical Me-SC junction. Here, ϕ_o is the so-called neutral level, above which the states are of acceptor type and below of donor type. This energy level is responsible for the surface pinning of the Fermi level on a free semiconductor surface, because when the Fermi level coincides with the neutral level at the surface, the net interface trap charge is zero. For a semiconductor with acceptor interface traps of density D_{it} states/cm²eV, constant in the range from $\phi_o + E_v$ to E_F , the interface trap charge density, Q_{ss} (C/cm²), is given by

$$Q_{ss} = -eD_{it}(E_g - e\phi_o - e\phi_{Bn}) \quad (2.32)$$

This quantity Q_{ss} , together with the space charge built up in the depletion layer Q_{sc} in equation (2.31) gives the total equivalent surface charge density

and an equal, opposite charge density $Q_M = Q_{sc} + Q_{ss}$ develops on the metal surface. The potential across the interfacial layer Δ of thickness d is found by applying Gauss law to the charge sheet, and also from the band diagram.

$$\Delta = \frac{-dQ_M}{\varepsilon_i} = \phi_m - (\chi + \phi_{Bn}) \quad (2.33)$$

Substituting for Q_M , this equation can be solved to find ϕ_{Bn} .

- When $D_{it} \rightarrow \infty$, then $e\phi_{Bn} = (E_g - e\phi_o)$ and the barrier height is entirely independent of ϕ_m , but solely determined by the surface properties of the semiconductor. The Fermi level is pinned by the surface states at $e\phi_o$ above the conduction band.
- In the second limiting case, $D_{it} \rightarrow 0$, the barrier height is $e\phi_{Bn} = e(\phi_m - \chi)$, which is the same as in the ideal Schottky case.

Empirical relations were found for many common semiconductors, among them GaAs. The barrier height for a metal-n-GaAs system was found to be $e\phi_{Bn} = 0.07e\phi_m + 0.51$, from this, $e\phi_o$ and D_{it} were obtained as 0.53eV and 12.5×10^{13} states/cm²eV [23]. The values of ϕ_o for most semiconductors are very close to one-third of the bandgap, which shows that these materials have a high density of defect levels near the neutral level. For most III-V compounds, it was found that the barrier height is essentially independent of the metal. This is also true for GaAs, where the barrier height is around 0.9V. Image force lowering of a barrier by $\Delta\phi$ is observed in the presence of an electric field [17] given by

$$\Delta\phi = \sqrt{\frac{eE_M}{4\pi\varepsilon_s}} \quad (2.34)$$

where E_M is the maximum electric field. In semiconductors $\Delta\phi$ is in generally small - in the order of 10meV - due to the high value of ε_s , but it still has a significant effect on current transport properties. The electric field due to the built-in potential is not a constant but a function of the surface potential. In effect, this means that for forward bias V_R the field and the image force are smaller and the barrier height is slightly larger than at zero bias, whereas at reverse bias the barrier height is slightly smaller. Controllable variation of the

surface barrier height is achieved by selective interface doping for example by ion implantation, in which case barrier height variation is not only achieved by the image-force lowering but more importantly via tunneling effects. For the right surface doping, tunneling and thus the saturation current density increases, due to high fields at the junction, effectuating an effective barrier reduction in the order of 100meVs. There are several theories to describe the current density -voltage relationship for a metal-semiconductor junction. One form of the current density, based on a combination of thermionic emission and diffusion theory [24] is given below:

$$J_{\text{TED}} = \frac{eN_c v_R}{1 + (v_R/v_D)} \exp\left(\frac{-e\phi_{Bn}}{kT}\right) [\exp\left(\frac{eV}{kT}\right) - 1] \quad (2.35)$$

where the relative values of the recombination velocity v_R and the diffusion velocity v_D determine the ratio of thermionic emission versus diffusion. $v_D \approx \mu_n E_m$ and $v_R = \sqrt{\frac{kT}{2m^*\pi}}$. In the limiting case that $v_R \gg v_D$, diffusion is the main limiting factor and for $v_R \ll v_D$, thermionic emission dominates. There is also a third contribution to the current which becomes important at low temperatures or in case of heavy doping: the tunneling current. The tunneling current is proportional to the quantum tunneling probability multiplied by the occupational probability in the semiconductor and the probability of unoccupied states in the metal. From experimental data, the total current density can be determined as a combination of thermionic emission and tunneling, and the most general expression is

$$J = J_o [\exp\left(\frac{eV}{\eta kT}\right) - 1] \quad (2.36)$$

where J_o is the saturation current density and can be found by extrapolating the current density from the J-V plot to $V=0$. η is the ideality factor close to unity at low doping concentrations and high temperatures. One can say that there is thermionic emission over the barrier, field emission near the Fermi level and thermionic-field emission in between. There exist complicated analytical expressions for each of these contributions, for more detail, see Chapter 3 of [17].

2.4.2 MIS structure and other contacts

When a thin interfacial layer of oxide is introduced on the surface, then a metal-insulator-semiconductor, MIS, system is obtained. The difference of MIS to the previously discussed metal-semiconductor case is that the interfacial barrier is thicker, with a potential drop of V_i across it and this results in a reduced majority current because of the additional interfacial layer. Fig. 2.15 shows the band structure of an ideal MIS structure in equilibrium. In an ideal MIS structure, the resistivity of the insulator is assumed to be so large that there is no dc current flow through the structure and the only charges that can exist are surface charges on the semiconductor and the metal. When a bias is applied, three possible configurations can exist at the semiconductor surface, as shown in Fig. 2.15. These three possible cases for an n-type MIS structure under external bias are accumulation, depletion and inversion. Accumulation occurs when a negative sample bias is applied, and is characterised by an enhanced density of electrons underneath the oxide. Depletion occurs at positive sample bias, the region below the oxide is depleted of electrons and a space charge zone is created. At even larger positive sample bias, inversion occurs, which means that the region below the oxide contains a high concentration of holes.

For an ideal MIS structure, the charge per unit area on the metal Q_M equals the charge per unit area on the semiconductor Q_s . The applied voltage appears partly across the barrier V_i and partly across the semiconductor depletion layer V_b . Following equations are valid:

$$V_{\text{appl}} = V_i + V_b \quad (2.37)$$

$$C_i = \frac{Q_s}{V_i} = \frac{d}{\varepsilon_i} \quad (2.38)$$

$$V_b = \frac{eN_D W_D^2}{2\varepsilon_s} \quad (2.39)$$

where C_i is the capacitance of the interfacial layer of thickness d . If the oxide is very thin ($d_{\text{ox}} = 1\text{-}3\text{nm}$), ideality does not apply and there is some tunneling across the barrier. The transmission probability according to [25] is given by

$$T = A \exp \left(-c \frac{d_{\text{ox}}}{V_i} [\phi_0^{3/2} - (\phi_0 - V_i)^{3/2}] \right) \quad (2.40)$$

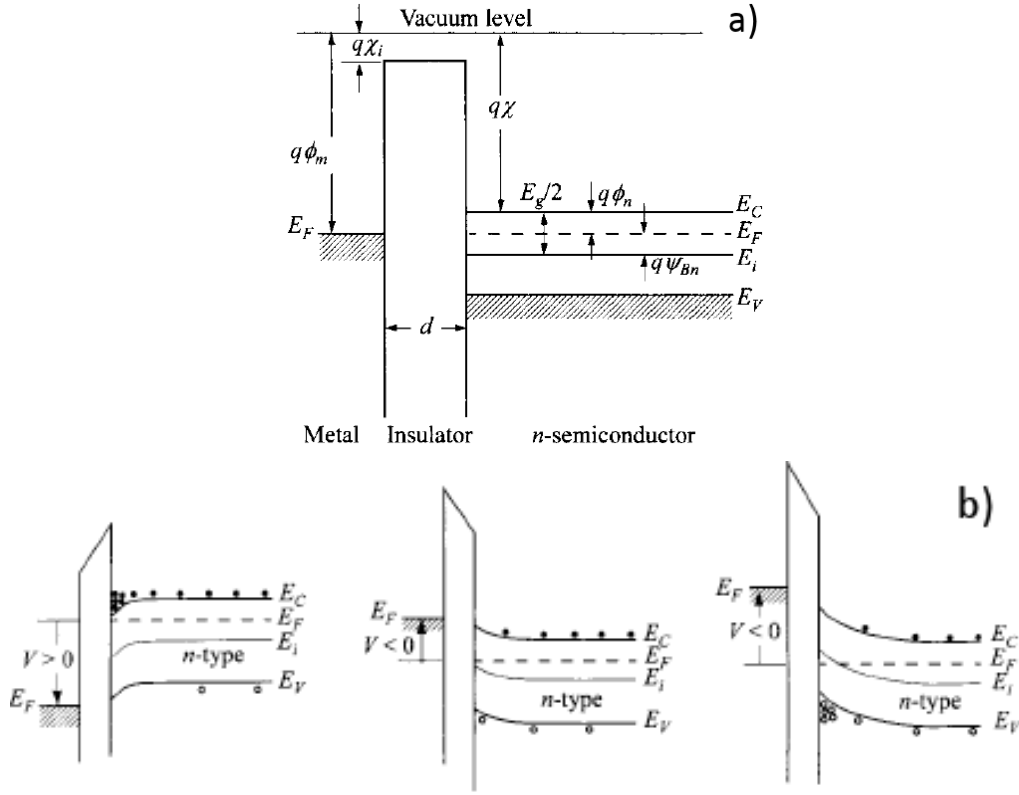


Figure 2.15: Band structure for an ideal MIS structure. a) in equilibrium, b) under applied bias, showing accumulation, depletion and inversion in this order.[17]

The current density can be described as

$$J = A_{\text{eff}} T^2 \exp(-\sqrt{\zeta} \delta) \exp\left(\frac{-e\phi_B}{kT}\right) \left[\exp\left(\frac{eV}{\eta kT}\right) - 1\right] \quad (2.41)$$

with the effective Richardson constant $A_{\text{eff}} = \frac{4\pi e m_{\text{eff}} k^2}{h^3}$. Not taking into account the change in the ideality factor (which is higher in the MIS case), this is just the same as before, in the direct metal-semiconductor case, with an additional barrier to overcome.

Point contact

If the metal makes a point contact with the semiconductor, this junction has less reliable current-voltage (IV) characteristics than planar devices, due

to variations in whisker pressure, contact area, surface condition and other parameters. The advantage of such a junction is a very small capacitance, the disadvantage a large spreading resistance and a large leakage current due to surface effects, moreover a soft reverse-breakdown due to the large concentrated field under the metal point.

Ohmic contact

There are also exceptions from the Schottky case: under the conditions of high doping concentration or low barrier height [26] the contact between a metal and a semiconductor can show Ohmic behaviour. Such contacts are characterised by a negligible junction resistance.

2.4.3 Charge carrier collection by the AFM tip

When the laser shines on the surface with the right energy, it delivers energy to excite electrons in the InAs QWells and QDots, as shown in the sketch below (Fig. 2.16). There are three basic mechanisms of how electrons can escape the confining QWells and Qdots: tunneling, phonon assisted tunneling and thermal activation. Once the charge carriers escaped confinement, the holes flow towards the tip and the electrons towards the back contact in the built-in electric field of the junction. The photocurrent that is measured is a sum of the hole current and the electron current. In order to collect more holes, it is possible to apply a reverse (sample) bias, which increases the band bending. Thus, the charge carriers can tunnel through a thinner barrier, plus their drift rate in a higher field is faster, facilitating the collection of more charge carriers, resulting in a higher PC signal. The only drawback of this approach is that thermally excited carriers are also collected, so not only the signal generated by excitation in the QDots and the WL but the background will also be higher. At forward bias, the band bending is reduced together with the drift velocity of charge carriers so the probability is high that they recombine before being collected by the AFM tip.

Fig. 2.17 shows the Schottky junction under various external bias conditions. The collection by the AFM tip thus results from the band bending due to the contact of a semiconductor with a good conductor. In our case,

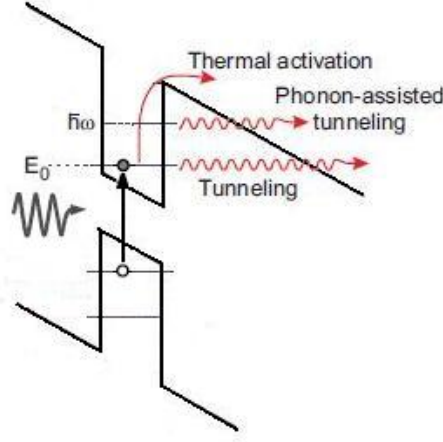


Figure 2.16: Excitation and escape mechanism from a quantum well.

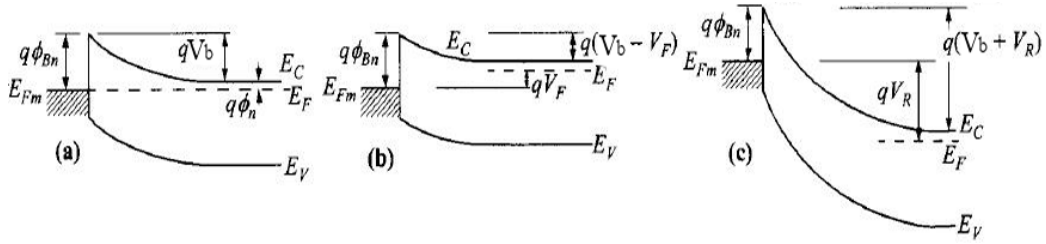


Figure 2.17: Schottky junction under various external bias conditions. a) no external bias, b) forward bias, c) reverse bias.[17]

the tip is not coated with metal but with a conducting, highly doped (p-type, $N_A=10^{20} \text{ cm}^{-3}$) conductive diamond layer. Such tips were supplied by NanoWorld. Diamond coatings are more resistant against abrasion and show under experimental conditions comparable behaviour to metal tips. The AFM tip acts as a sink for charge carriers, it introduces - even under zero external bias conditions - an additional radial field as shown in Figure 2.18. This area constitutes the detector volume for our system. The colour scheme for the potential ranges from white for a positive potential through rainbow colours towards black for a negative potential. The depth of this collection region is about 150nm, which correspond to the depth to which our samples are intrinsic. This distance is shorter than W_D discussed above, since the depletion region effectively ends together with the intrinsic region.

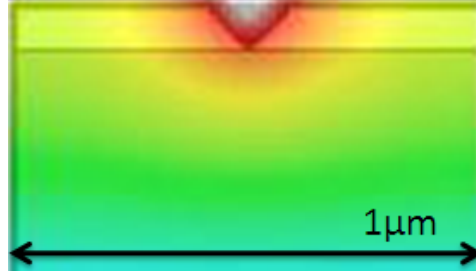


Figure 2.18: Potential distribution under an AFM tip assuming Schottky contact between tip and surface. Adapted from [27].

The lateral dimensions of the collection area are approximately 200x200nm, as it can be seen from the simulated potential distribution, which is much smaller than the area illuminated in our setup. To see that this area is a reasonable size for generating enough charge carriers to give a 10pA signal, the number of charge carriers generated by illumination in the WL were calculated, taking a box of 200x200x2nm. This should give a current of about 1nA, assuming that all charge carriers are collected by the tip. This is a reasonable assumption, because the distances the charge carriers can travel during their lifetime are even higher, somewhere in the μm range.

2.5 Dependence of PC on experimental parameters

2.5.1 Wavelength and intensity of incident light

Assuming normal incidence and minimal reflection losses at the surface, the incoming light is transmitted through the sample with exponentially decaying intensity depending on the absorption coefficient α . Our experiments are carried out in a wavelength range 870nm-1300nm, corresponding to an energy range of 1.42-0.95eV. This energy range is below the GaAs bandgap, therefore the absorption coefficient α_{GaAs} is zero and there is no absorption by GaAs in this spectral region. The absorption coefficient of InAs at room temperature has a plateau around this spectral region, with values in the order of 10^4 cm^{-1} . From the Beer-Lambert law of absorption $I = I_0 \exp(-\alpha x)$

the absorption in a thin layer of InAs of thickness 2nm, can be calculated to be about 2% of the incident light intensity, with a negligible increase towards higher energies. Assuming a photoexcitation efficiency of 100%, which means that all incoming photons excite an electron and reach the contact, the photocurrent intensity can be calculated to be around 2nA. This assumption is reasonable since we are working at high temperatures and fields, and can expect carrier velocities around 10^6 cm/s, which is fast enough for the carrier to be extracted from the detection volume faster than it can recombine. 100% photoexcitation efficiency was also suggested by [1] under similar experimental conditions. The calculated current is in the same order of magnitude than the photocurrent measured experimentally with the PC-AFM setup. As the variation in α_{InAs} is negligible, only the variation of incoming light intensity is expected to have an influence on the photocurrent signal. Under the assumption of 100% generation, the PC signal is directly proportional to the incoming light intensity.

2.5.2 Doping and surface states

The InAs layer where the charge carriers are generated by optical excitation and the neighbouring GaAs layers constitute the intrinsic region of our Schottky-i-n photodiode structure. Dopant concentration influences the charge carrier mobility, and thus also determines the current density of the sample as well as the width of the depletion zone, the magnitude of the electric field and consequently also the magnitude of the surface barrier. Higher doping leads to larger mobilities, reduced depletion widths and surface barriers. The depletion region constitute the detector volume for our sample, so reduction in the depth of the depletion region would lead to a reduction of the nominal detector volume. However for our case, as long as the electric field extends into the depth where the InAs layer is located (130nm) we can assume that all photoexcited carriers reach the AFM tip. This is true for charge carrier densities smaller than $5 \times 10^{17} \text{cm}^{-3}$.

Surface defects are always present on native GaAs surface and result in surface pinning induced band bending as discussed before. They also play an important role in the barrier formation at the tip-sample contact. If

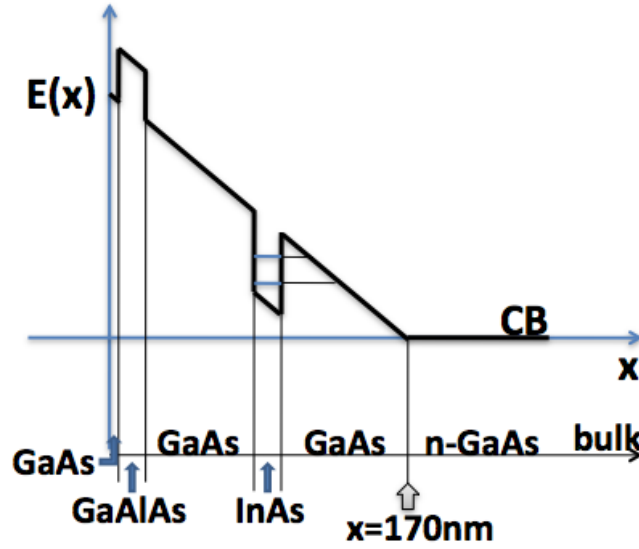


Figure 2.19: Schematics of the conduction band near the sample surface.

the surface states are saturated, for example by means of a lattice matched thin aluminium oxide layer deposited on the surface, then flatband condition can be achieved. In this case, there is no tunneling at zero external bias. Under reverse bias, band bending occurs as shown in Fig. 2.19 and tunneling becomes again possible. Comprehensive information on interface states on GaAs and the calculation of the resulting Schottky barrier height can be found in [28].

2.5.3 Voltage

At zero external bias the built-in voltage at the sample surface corresponds to the magnitude of the band bending, i.e. to the slope of the curve in Fig. 2.19. When an external voltage is applied, it changes the position of the Fermi level in the semiconductor and has the effect of lowering the barrier at sample bias (positive voltages) and increasing the barrier at tip bias (negative voltages). It also changes the extensions of the space charge region parallel to the sample surface. In the direction perpendicular to the surface, the space charge region ends at the highly n-doped layer at a depth of 190nm. The slope of the curve defines the tunneling probability according to equations 2.23 and

2.24. To put it very simple, the tunneling probability is proportional to the width of the barrier. At higher fields, the slope is steeper and the barrier width for a given energy level in the quantum well smaller and carriers can escape the quantum well more easily. Typical electric fields for our sample are in the range of 50kV/cm. Due to the presence of surface states and/or a metal contact, there is a band bending and a built-in electric field close to the surface, so at zero external bias, photocurrent can be measured. By applying a forward bias the barrier can be lowered until the built-in field cancels out. Under flatband conditions, the photogenerated carriers cannot escape the InAs quantum well, there cannot be any net charge flow and thus there is no photocurrent response.

2.5.4 Pressure

The bandgap of semiconductor materials depends on the pressure P [kbar] according to [29]

$$E_g = E_g(0) + 4.8 \cdot 10^{-3} P \quad \text{for InAs} \quad (2.42)$$

$$E_g = E_g(0) + 0.0126 P - 3.77 \cdot 10^{-5} P^2 \quad \text{for GaAs} \quad (2.43)$$

This can be explained by thinking that at high pressures, the atoms are forced to move closer together, resulting in larger spacing of sites in reciprocal space and a larger spacing of energy levels. The tip exerts high pressure in one point only, which presumably results in an inhomogeneous compression of the topmost atomic layers under the tip. The pressure under the tip calculated for a setpoint of 1V and a cantilever spring constant of 42N/m is in the order of a few GPa. Assuming a pressure of 10kbar, the increase in E_g is for InAs is about 50meV and for GaAs about 120meV. However, this influence only affects the topmost layer of the material and does not reach the InAs wetting layer so there is no observable shift in the photocurrent spectrum. Also, at high pressures the tip penetrates deeper into the surface, thereby increasing the contact area to the sample. Therefore under high pressure conditions, higher currents can be expected. Changes in the tip pressure lead to changes in the photocurrent signal.

2.5.5 Temperature

The temperature dependence of the bandgap for InAs and GaAs according to [29] is given by

$$E_g = 0.415 - 2.7610 \cdot 10^{-4} T^2 / (T + 83) \quad \text{in eV for InAs} \quad (2.44)$$

$$E_g = 1.519 - 5.405 \cdot 10^{-4} T^2 / (T + 204) \quad \text{in eV for GaAs} \quad (2.45)$$

which means that at higher temperatures the bandgap gets smaller, resulting in a reduction in the energy separation of VB and CB sublevels and a redshift of the spectral features related to the InAs layer in the emission and absorption spectra. The variation of the energy gap of InAs with temperature is shown in Fig. 2.20

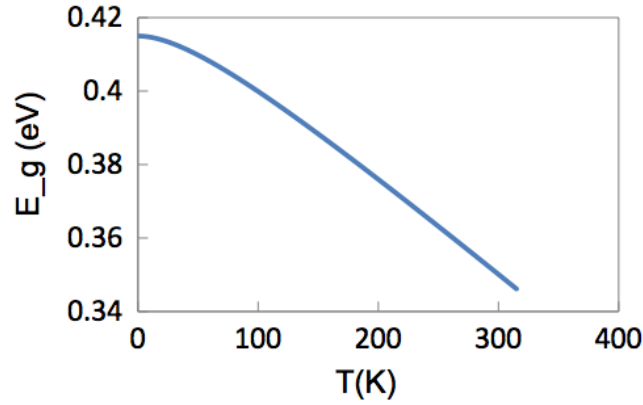


Figure 2.20: Energy gap of InAs as function of temperature.

Chapter 3

Experimental Considerations

In the following sections, first the sample used for testing the photocurrent (PC) setup is introduced, then the working principle of an AFM and its applicability to photocurrent measurements is briefly explained. This is followed by the description of the PC setup, comparing the parameters of the initial setup containing a halogen light source to the new setup using a broadband laser source. The laser setup performs better with respect to measurement times, signal intensities and spectral accuracy. Finally some general trends in the photocurrent behaviour, like pressure and voltage dependencies, are explained.

3.1 Samples

To test the performance of the localised PC measurement setup with an AFM, we measured the PC on self-assembled InAs quantum dot samples. The layer sequence of the samples is shown in Fig. 3.1. The samples were fabricated by molecular beam epitaxy (MBE), by first depositing a highly doped GaAs:Si layer on the n-type GaAs substrate and subsequently growing intrinsic GaAs, with a thin 0.7nm layer of InAs sandwiched in-between. On top, a GaAlAs blocking layer was grown to reduce surface recombination of photogenerated carriers, then the surface was capped by 10 nm GaAs to avoid oxidation of the GaAlAs layer. For one of our measurements, a sample without a blocking layer was used, with a thin layer of Al₂O₃ deposited

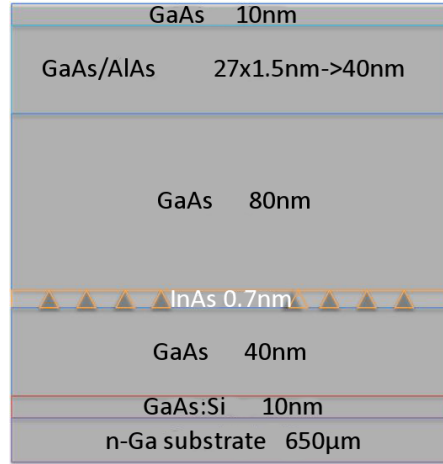


Figure 3.1: The layer sequence of the H269 quantum dot sample.

instead. For our PC measurements, the back contact is realised by alloying InSn pellets into the sample at 450°C for 5 min. The InSn diffuses through the sample creating a highly n-doped conduction pathway to the back of the sample. Conductive silver was used to glue gold wires to the InSn pellets and make the contacts.

3.2 CAFM and its use for PC measurements

The atomic force microscope (AFM) was developed to measure a topographical image of the sample by monitoring the forces between tip and sample surface. To do this, a sharp tip mounted at the end of a flexible cantilever is traced over the surface and a constant force between tip and sample is maintained. As the tip encounters surface features, it gets deflected and this deflection can be monitored by means of a laser beam which is reflected from the back of the cantilever and detected by a special 4 quadrant photodetector. Based on this deflection signal, the force on the cantilever is readjusted and the image is obtained, as it can be seen from the schematics in Fig3.2. This mode of operation is called contact mode and it works well for hard, homogeneous materials. The other two main operation modes of the AFM are the tapping mode and the non-contact mode. The tapping mode is frequently applied when scanning soft surfaces. Here, the AFM tip only touches

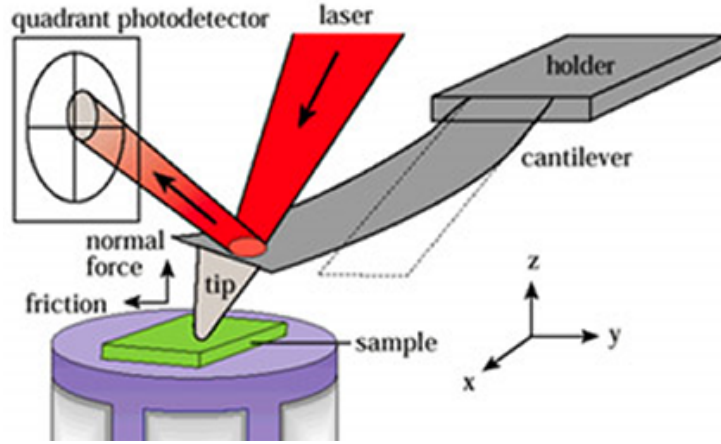


Figure 3.2: Schematics of an AFM tip and feedback.[30]

the surface from time to time, minimizing the impact on the sample. The non-contact mode is especially useful to get information about other factors than topography, i.e. elastic modulus of the sample or forces between tip and sample. Since the invention of the AFM, a whole family of different applications appeared for this instrument, as mentioned in the introduction. For us, conducting AFM (CAFM) is the most interesting method, which is realised by using a conducting tip and monitoring the current flow [31]. When measuring the PC in a sample with the AFM tip, we want to record a complete spectrum in one spot before moving to another sample location. By touching the tip to the surface using a constant pressure, the AFM tip can be kept in place so the variations in the current only stem from the photogenerated charge carriers that are collected. A constant contact force is important in this case, because we are mostly working with hard, diamond coated cantilevers, that penetrate into the surface at higher contact forces, thereby changing the contact area between tip and sample.

3.3 Setup for PC measurements

Fig3.3 shows a schematic diagram of our measurement setup. The AFM used is PicoPlus made by Molecular Imaging, with current sensing extension. A central personal computer with LabView interface controls the two circuits

and the monochromator.

The first circuit is the AFM feedback and control loop, which is used to position the tip, set the contact force and maintain a stable contact between tip and surface by controlling the piezo scanner. The other circuit has the purpose of measuring the PC, and is connected to the AFM tip and the back of the substrate. PC measurements are carried out using a Keithley 6430 source measure unit (SMU) that is capable to detect very small currents. The zero offset of our SMU was 162fA, this means that any PC curve measured was shifted upwards by this value.

In addition, there is also a third "circuit", which is just the optical pathway for the sample illumination. White light from the light source is fed into the Triax180 JobinYvon monochromator controlled by the program that selects the required wavelength. The image of the spectral band at the exit slit is then focused onto the end face of a glass fiber and used to illuminate the sample. The monochromator uses a plane grating with 1200 lines/mm and has an inverse linear dispersion of 7.2nm/mm. The achievable spectral bandwidth is given by the linear dispersion times the slit width, which means that for our monochromator a spectral bandwidth of 7.2nm can pass through a slit width of 1mm. By reducing the slit width, the output bandwidth can be reduced at the cost of the intensity. From this, it can already be anticipated, that in order to get good resolution, the limiting width (either the exit slit or the width of the fiber) needs to be small and only allow a narrow band of wavelengths to pass through. However, reducing the limiting width also reduces the output intensity, so in general, a compromise between intensity and bandwidth needs to be found.

In order to get a stable AFM feedback signal, shielding from ambient light, vibration isolation and temperature control are the most important things to consider. Our setup is in a dark box mounted on a vibration isolation table and additionally protected by a polystyrene foam from influences of sound. Temperature control is necessary because of the different heat expansion coefficients of the materials in use. As parts of the setup change their length as a response to temperature, the cantilever drifts uncontrollably over the surface. Therefore it is very important that the setup is in thermal equilibrium when starting a measurement. Temperature control is

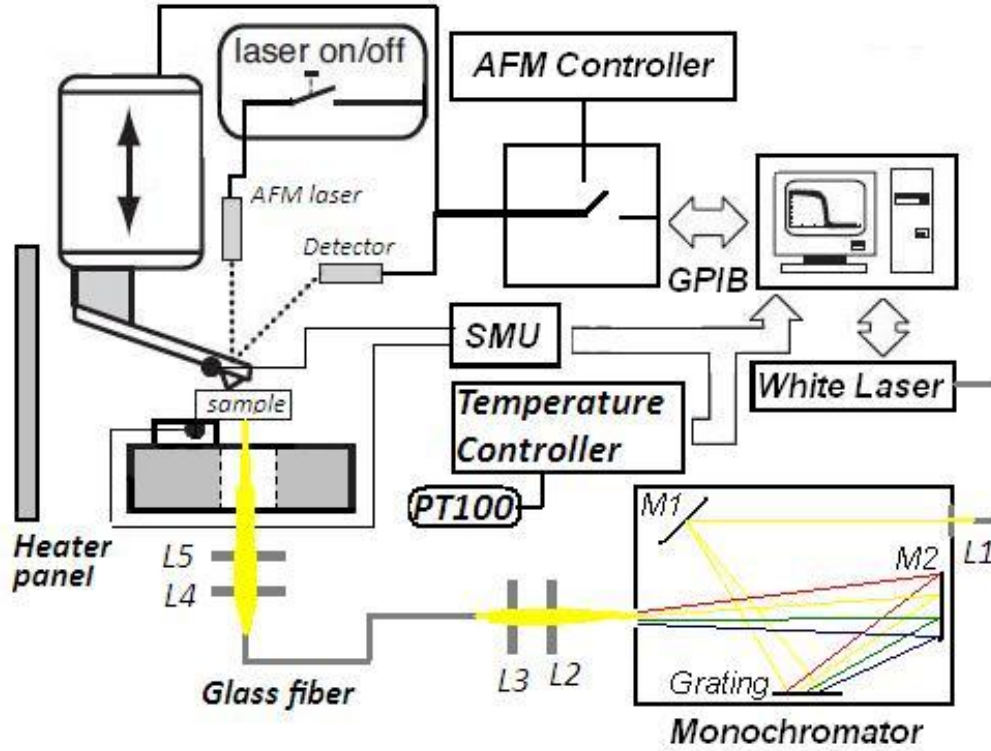


Figure 3.3: Schematics the measurement setup.

achieved by a heater connected to a temperature sensor in a feedback loop, so that a reasonably constant temperature is maintained in the insulation box - temperature fluctuations in the order of mK. Since we are measuring very weak current signals, strong external electric fields and static charging can also pose a problem, as well as cable capacitances. To shield the setup against these influences, a conducting tin foil layer is protecting the interior of the measurement box. Cable capacitances are dealt with by using short coaxial cables and monitoring the signal and waiting for a stable response.

Fig. 3.4 shows a picture of our measurement setup, which stands on a laser table. The heater for the temperature control and the optics for focusing light onto the sample can be seen. The LabView control program is responsible for setting the wavelength, switching the AFM laser on and off and recording the PC values. The main parameters are averaging parameters for the PC signal, the delay times before and after measurements and the

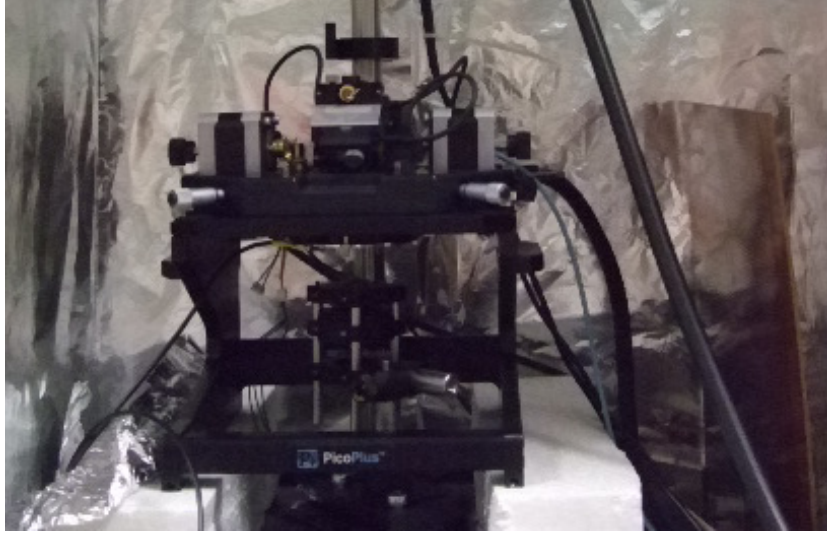


Figure 3.4: The setup for measuring photocurrent. The AFM, the contacts to the SMU and the focusing optics are shown.

stability of the error signal, which indicates the stability of the tip-sample contact.

3.3.1 Lightsource 1

In the initial setup, a halogen lamp was used as a light source. Its light was lead through a monochromator that separated out a narrow band of wavelengths through the exit slit. This band of wavelength was then focused into a multimode glass fiber with a diameter of about 5mm, that lead the light to the AFM and illuminated the sample from below in a manner that the end of the fiber was almost touching the back of the sample. The illuminated area was in the order of 15mm^2 . The AFM tip was in contact with the sample at the top, and a contact force of about $10\mu\text{N}$ was applied. The spectral power as emitted from the monochromator at a slit width of 5mm - corresponding to a transmitted wavelength band of 36nm - is shown in Fig.3.5. The intensity increases from the low wavelength end towards the high wavelength end of the spectrum and levels off after 1300nm.

However, illumination by means of a halogen lamp showed certain shortcomings. The first problem was the low intensity of light incident on the

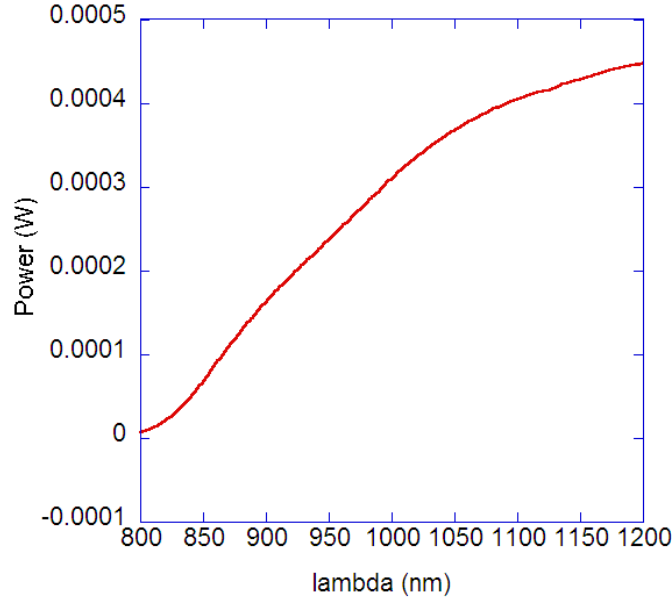


Figure 3.5: Reference spectrum of the halogen lamp showing the relative intensity transmitted by the monochromator for each wavelength.

sample, from the reference spectrum of the halogen lamp it can be seen that typical intensities range from 0.1mW to 0.4mW. The AFM feedback laser, on the other hand, provides about ten times higher intensities at a constant wavelength of 633nm, which generated carriers in GaAs and InAs alike and disturbed the measurements. This was solved by using an intercepted feedback loop [32], periodically switching the AFM laser on and off for each measurement point, as illustrated in Fig. 3.6.

The photocurrent was measured during the OFF period and during the ON period, the piezo feedback could regain and maintain a reasonably constant tip-sample contact. When the AFM laser was ON, the error signal of the piezo was recorded, averaged and when the laser was off, this average error signal was fed into the system, in order to keep the cantilever in a stable position. This way, reliable measurement data could be obtained, but this procedure also resulted in prolonged measurement times. Instead of measuring in a time t_{OFF} and then moving to the next spectral position, the measurement lasted about twice as long, $t_{\lambda} = t_{\text{OFF}} + t_{\text{ON}}$. Photocurrent signal intensities obtained were in the range of about 1 picoamps at best, which

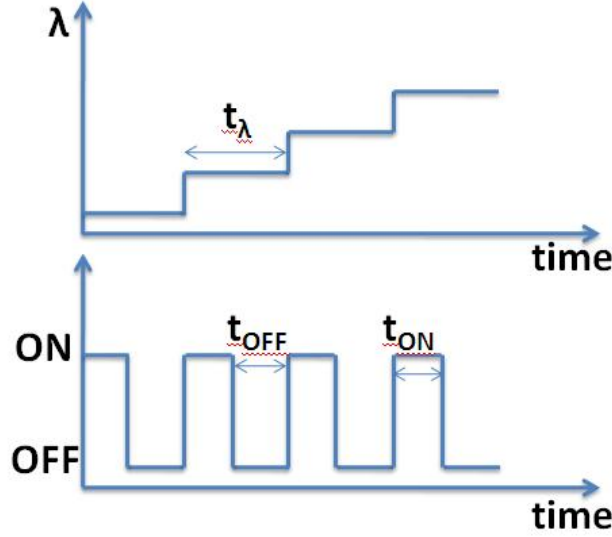


Figure 3.6: Sample illumination and effective measurement time.

was attributed to the low illumination intensity.

Long measurement times for a spectrum introduce an additional requirement: temperature stability. All components of the AFM need to equilibrate at a certain temperature in order to avoid mechanical stresses and strains due to different expansion coefficients. If the equipment is not completely equilibrated, tip drifts over distances of 100nm are possible during a measurement that lasts about 40 minutes. Even if the setup is equilibrated, some slight drifting of the tip cannot be ruled out.

Another problem was the insufficient wavelength resolution. Light diffracted from the grating inside the monochromator shows a linear wavelength dispersion of 7.2nm/mm and if an exit slit of 7mm is used, this gives a bandwidth of about 50nm for light incident on the sample surface. The slit width could not be further reduced to improve accuracy, because the remaining intensity would not have been sufficient to create a measurable PC signal. This made it extremely difficult to interpret the spectra with respect to any quantum dot levels, which were smeared out and hard to identify over the noise.

The area of illumination was in the range of mm^2 , and since the dot density was about 30dots/ μm^2 , many many dots were affected by the incoming

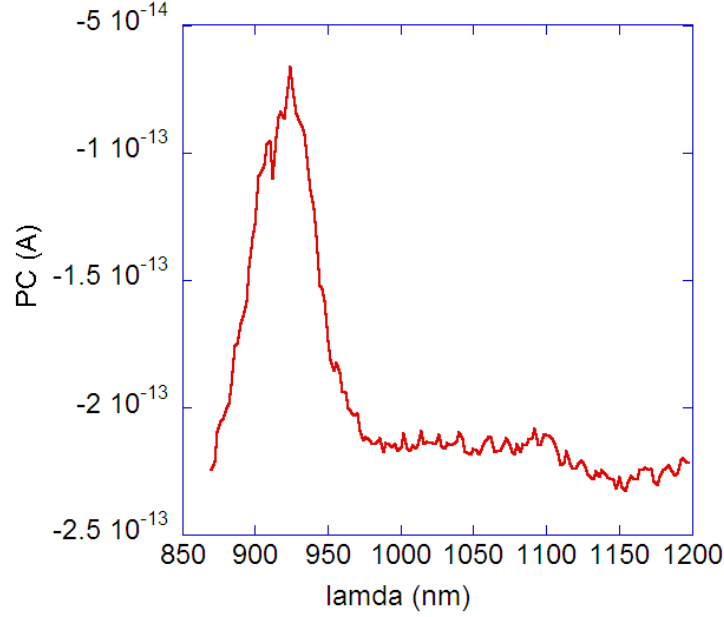


Figure 3.7: Typical PC spectrum of an InAs quantum dot sample recorded with a halogen lamp as light source.

light. This fact on its own does not determine the spatial resolution because the collection area is determined by the diffusion length of charge carriers in the vicinity of the tip. Simulations suggest that the collection area for charge carriers around the tip is in the range of $200 \times 200 \text{ nm}$ [27], which means that only one dot can be probed at the time. Thus the greatest limitation of the setup with the halogen lamp is the insufficient intensity and the poor wavelength resolution. Fig. 3.7 shows a typical PC spectrum as obtained by the old setup. The peak resulting from the thin InAs layer near the surface, the so called wetting layer, that effectively forms a quantum well, is clearly visible at $\lambda_{\text{WL}} = 920 \text{ nm}$. The full width at half maximum of the wetting layer peak is 50 nm . The maximum photocurrent obtained is about $0.2\text{--}0.5 \text{ pA}$, other features in the spectrum are in the 1 fA range. The tiny bump at 1100 nm could represent a quantum dot energy level or an artefact possibly caused by vibrations.

There is always a current signal at $\lambda > \lambda_{\text{WL}}$, even if no individual QDot peaks are observed. Possible explanations for this background current are

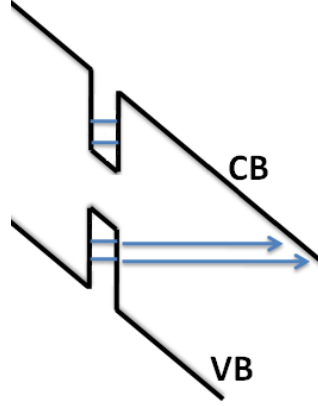


Figure 3.8: Tunneling at high fields across bandgap as possible explanation for photocurrent background.

listed below.

- Direct tunneling from the VB into the CB at high fields as shown in Fig. 3.8 would allow for transitions at several different energies. The fields at the AFM tip at a bias of 1V are in the order of 20kV/cm, which might be enough to explain such effects. However it is questionable whether the band bending under zero bias conditions is sufficient to induce this effect.
- Broadening of peaks due to reduced surface lifetimes is another possible explanation for the background signal. However, our samples were fabricated with an AlGaAs blocking layer in order to counterbalance this effect.
- Another hypothesis is that due to the size distribution of the dots, their energy levels are shifted with respect to each other. So if the current collection region includes 3 QDs, the peaks will all be at different positions. Taking into account the broadening due to the low spectral resolution, this could also create a smeared out PC background. It seems that only dots in the immediate vicinity of the tip show up as prominent features in the spectrum.

3.3.2 Lightsource 2

In order to enhance signal intensity and obtain better wavelength resolution, a broadband laser light source of make Koheras Versa was implemented in place of the halogen lamp. Most lasers operate at one fixed wavelength, but in recent years, broadband laser sources have been developed, where a seed laser radiates through a photonic crystal and excites a wide range of wavelength that are then emitted together with the seed wavelength. The spectral output of these lasers is very stable and constant over a wide range of wavelengths.

The laser light was dispersed by a lens before entering the monochromator through the entrance slit. This is important because the non-dispersed layer beam is strong enough to damage the diffraction grating in the monochromator. After passing through the monochromator the diffracted beam arrives at the exit slit. The exit slit is imaged by a lens system onto the end of a glass fiber with $200\mu\text{m}$ diameter. Only a $200\mu\text{m}$ portion of the total spectral band that exited the monochromator is coupled into the fiber. According to equation 2.11 the bandpass is given by the limiting width ($200\mu\text{m}$) times the inverse linear dispersion (7.2nm/mm). Inserting the numbers gives a bandpass of 1.44nm , which is the resolution of the improved system. This is a more than 20fold increase in spectral resolution of the setup compared to the achievable resolution by the old setup with the halogen lamp. Even though a much smaller section of the output wavelength band is used to illuminate the sample, the output power measured at the end of the glass fiber is in the range of 2mW , which is on average tenfold higher than the power output in case of a halogen lamp.

There is only one problem, which is the strong presence of the seed laser peak in the output spectrum as can be seen in Fig3.9. The spectrum looks identical recorded through a GaAs wafer and in air. This proves that shining the laser through the wafer does not significantly influence or attenuate the light that excites the electrons of the InAs quantum well (wetting layer) and the quantum dots.

A typical PC spectrum of the quantum dot sample is presented in Fig. 3.10 below. The wetting layer peak is clearly visible with a peak height of

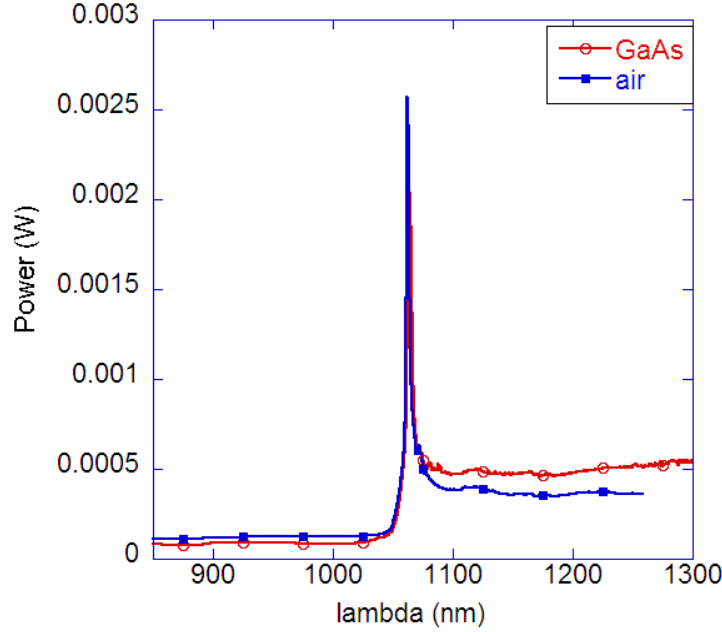


Figure 3.9: Reference spectrum of the white laser recorded through a GaAs wafer.

12pA, but there is a second prominent peak in the spectrum at 1062nm with a peak height of almost 15pA, that results from excitation by the seed laser with much higher intensities than at other wavelength. The fact that the seed laser peak is so prominent also suggests, that there are quantum dot levels or the possibility of some other excitation mechanism, like for example interband tunneling around these energy levels. Fig 3.10 above was recorded while switching the AFM laser off to ensure that it cannot interfere with the measurements. As the broadband laser has a much higher intensity than the AFM laser, spectra were also recorded leaving the AFM laser on and thereby reducing measurement time by a factor of 2. For comparison, Fig3.11 shows both the "original" spectrum, where the AFM lasers was switched on and off, and the spectrum recorded while the AFM laser was kept on.

The difference in the signal intensity at the wetting layer peak can be attributed to the location dependence of the photocurrent. The thickness of the wetting layer under the tip, the tip pressure, and the presence of moisture can all influence the photocurrent signal. In general, the first spectrum shows

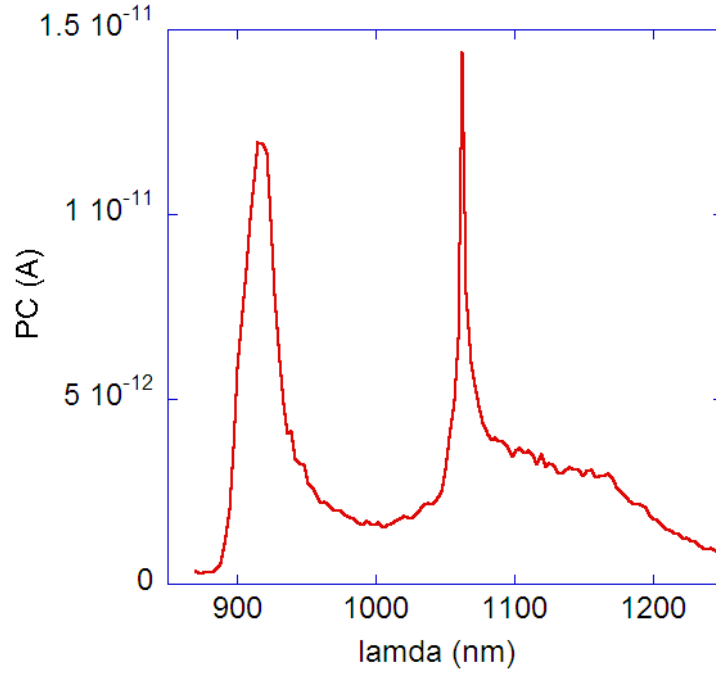


Figure 3.10: PC spectrum of an InAs quantum dot sample recorded using the white laser as light source.

lower signal intensities than the following spectra. One possible explanation is that during the first run the tip penetrates the surface until a certain depth is reached. Measurements always show the same overall characteristics, but signal intensities vary slightly with each measurement. The difference in the spectra around 1150nm is much harder to explain. The AFM laser operating at 633nm should not have an explicit influence at 1150nm.

Observing the above spectra, it appears that there are no QDot levels with strong intensity, despite the fact that the spectra show a much higher spectral resolution than before. Unfortunately, we did not measure any spectra with peaks that could be attributed to the contribution of the QDot levels. This might be due to the low density of QDots (about 30dots/ μm^2) in the sample, which makes the probability to hit one by the AFM tip quite low, about 4%. We believe that small bumps indicate the influence of nearby QDots on the PC signal, this is supported by photoluminescence measurements and will be discussed in the next chapter. There is another point to mention about

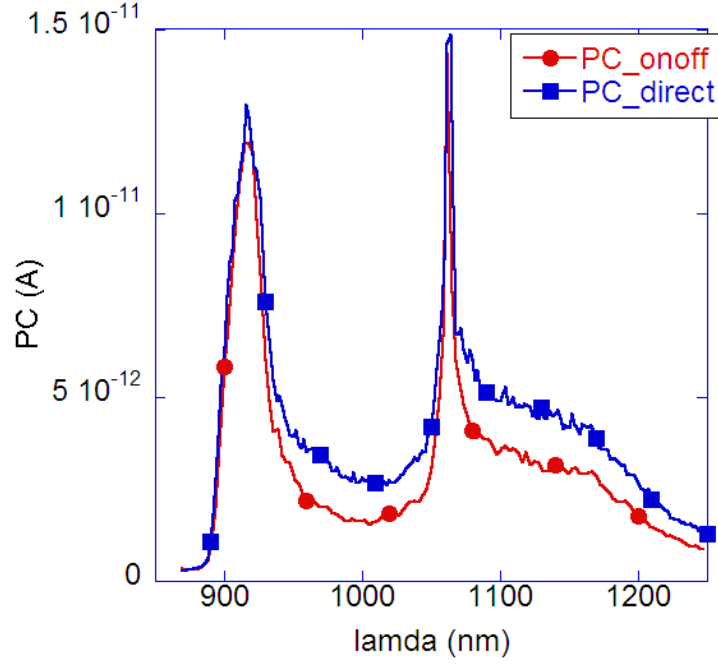


Figure 3.11: PC spectrum of the H269 InAs quantum dot sample recorded with the AFM laser on during the measurement (squares) and with the on/off feedback (circles).

wavelength resolution: although we now have a bandwidth of about 1nm and therefore we know the exact relative position of our spectral features, the assignment of the absolute spectral position could be about 5nm off, due to the fact that we are selecting the brightest 200 μm part of the 1mm image of the slit when coupling into our 200 μm glass fiber.

A useful feature of the white laser is that it is possible to switch the booster module on and off and so quasi-simultaneously record a PC spectrum and a dark current spectrum. For this, at each wavelength the sample is first illuminated and the current is measured, then the booster is switched off and the current is measured again. This shows in comparison that we are measuring true photocurrents. Unfortunately, the booster module only switches wavelength away from the seed laser wavelength. The seed wavelength is still coming through when the booster module is switched off. Nevertheless, it can be seen from Fig 3.12 that at all other wavelength the dark current is

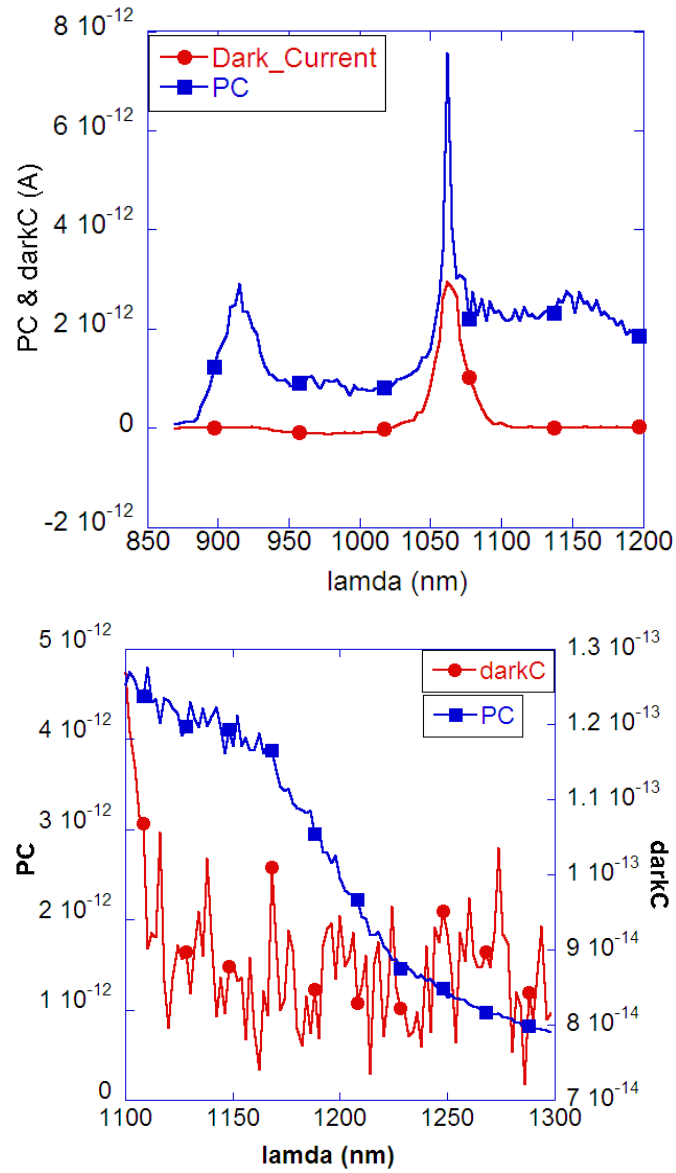


Figure 3.12: Comparison of the photocurrent response with the dark current response. The complete spectrum (top) and a magnified section of the spectrum are shown.

negligible and that the fluctuations do not correlate with features in the PC signal. Thus we can claim that we are measuring a true photocurrent signal with our setup.

The main advantages of the laser excitation source as compared to the halogen lamp are the following:

- Shorter measurement times: With the halogen lamp, 110 measurement points could be recorded in 40 minutes and with the white laser 165 measurement points within 15 minutes. This is a 4-fold increase in measurement speed in favour of the new setup. The fact that measurements are 4times faster also means that possible drift is on 4times shorter length scales than it was before.
- Higher PC signal intensities: The photocurrent intensity obtained at λ_{WL} increased tenfold, typical intensities of the wetting layer peak are in the range of 10pA. Unfortunately, we did not observe any QD levels. The noise in the photocurrent is in the order of 0.5pA, and possibly a result of the averaging routine of the SMU.
- Significantly improved wavelength resolution: besides the gain in measurement time this is the main advantage of the new setup. The exact position of any spectral feature can be found, provided that the absolute positions are calibrated using the known position of the seed laser peak. The better spectral resolution allows for the discovery of new features, like the sub-structure of the wetting layer peak.

There is also one drawback:

- The strong presence of the seed laser peak at 1062nm obscures the central part of the spectrum. Radiation at these wavelength is so intense, that it also interacts with the AFM photodiode, disturbing the feedback. An ultra-narrow bandpass filter could however solve this problem.

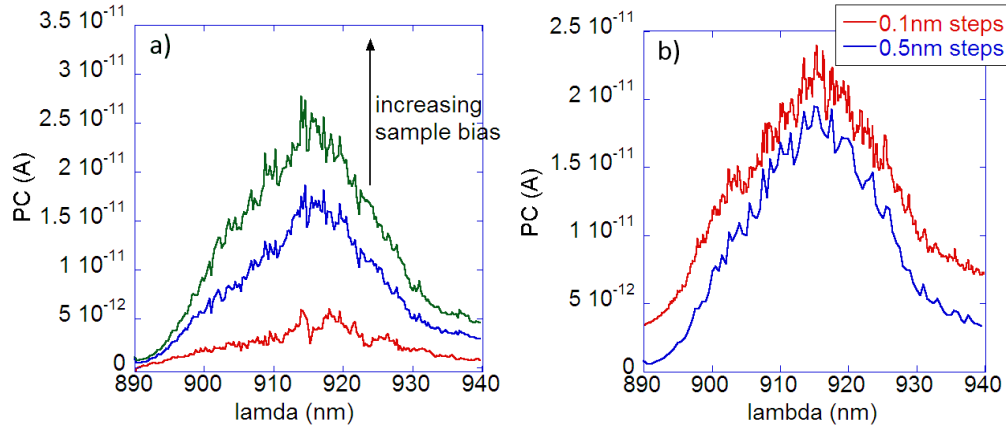


Figure 3.13: Fluctuations of the PC signal. a) voltage dependence of the fluctuations b) dependence on the number of measurement points.

3.4 Characteristic behaviour of PC spectra

3.4.1 Wavelength resolution

The wavelength resolution depends either on the exit slit width or the resolution limit of the monochromator. In our case, only a $200\mu\text{m}$ wide band of the exiting light is coupled into the fiber, corresponding to a bandwidth of 1.44 nm. The wavelength resolution specification for our monochromator is 0.2 nm. Still, within the software, it is possible to choose arbitrary wavelength resolution. The smaller steps are chosen, the more measurement points are recorded. The spectra in Fig 3.13 show fluctuations in the measurements that are proportional to the signal intensity and more fluctuations appear for more measurement point. Therefore we believe that these artefacts are a result of the internal signal acquisition cycles of the SMU an optimisation of parameters would be useful to reduce this effect. Our maximum attainable resolution could be improved by using a thinner optical fiber but this would only be useful after optimising the SMU signal, because at the moment, fluctuations are on the nanometer scale.

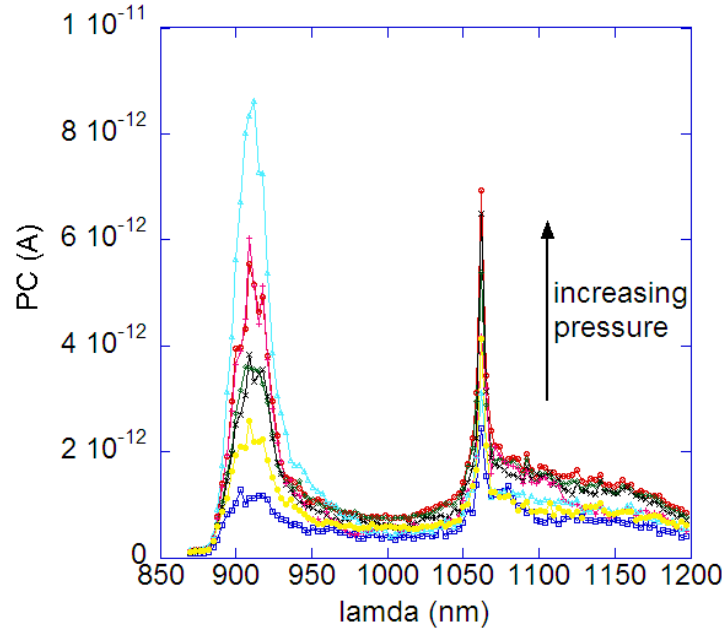


Figure 3.14: Pressure dependency of photocurrent spectra.

3.4.2 Pressure dependent behaviour

The spectra recorded at different pressures show the following trend: When a larger contact force is applied, the PC signal increases. This can be explained by realising that the surface is never completely clean since we are working in a normal laboratory environment and so at very light forces, there very likely is an additional barrier from the surface debris or water film that the charge carriers have to overcome. As the force is increased, the tip penetrates deeper into the surface, thereby increasing the contact area to the surface and assuring a good tip-sample contact. Once a good contact is established, the PC remains high even when the contact force is reduced until the tip is withdrawn. Another mechanism that plays an important role in this case is the high pressure applied to the sample. Pressures are in the range of 4GPa, which is enough to compress the topmost layers of atoms and thus reduce the Schottky barrier.

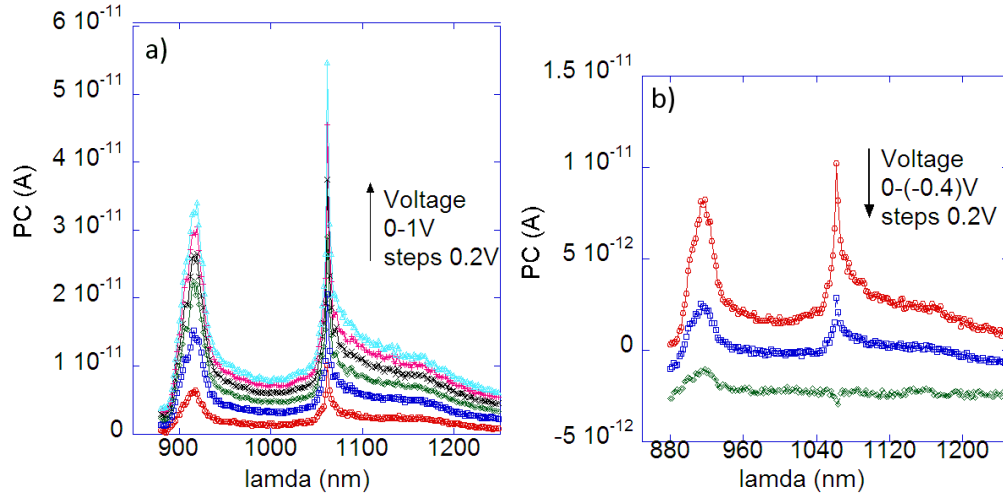


Figure 3.15: Voltage dependency of PC spectra. a) forward bias, b) reverse bias.

3.4.3 Voltage dependent behaviour

Fig 3.15 shows the voltage dependent behaviour of the photocurrent signal of a H269 sample without surface oxide. As it can be anticipated, the signal increases with a positive sample bias (reverse direction) because more charge carriers can be collected in the resulting stronger electric field (principle explained section 2.5.3). This enhanced collection is mostly due to steeper bands, where charge carriers can escape their confinement -QWell- more easily due to thinner tunnel barriers. The drift velocities are also higher, which should increase the collection area.

When a forward bias (negative sample bias) is applied, signal intensities decrease dramatically. At voltages higher than -0.5V, no more features can be observed and current flow is dominated by electrons injected from the voltage source, collected by the tip. Photogenerated carriers can hardly escape the QWells any more because the bands are essentially flat due to the voltage applied. The Schottky barrier height seems to be about 0.5V and is counterbalanced by the external voltage. There is one interesting feature to observe in the spectrum, which is the drop in the current just after the seed laser wavelength at an applied voltage of -0.4V, while the WL signal still appears as a peak. The most likely explanation for this is that at -0.4V, there

is still some band bending and resultant electric field in the region close to the surface, where the QWells are located. So some charge carriers generated in the wetting layer can still escape the QWell, yielding the small peak at a wavelength typical for the WL. However, under high illumination conditions, band bending is affected by the many photogenerated charge carriers. This could lead to a further decrease of the barrier and a temporary current flow in forward direction until the excess charge is released.

Positive sample bias can be used to enhance the PC signal of dot levels, the highest curve recorded at 1V clearly shows the most pronounced peaks in the 950-1050nm and 1070-1200nm region. The peak width is less than 10nm, but the peak intensities are only about 2pA, which suggest that there were no QDs in the immediate vicinity of the tip, only at the edge of the collection region. Due to the stronger field, not only photogenerated but also some thermally excited charge carriers are collected, which appears as a non-zero current signal below the wetting layer peak, where there aren't any levels available for photoexcitation. At the high wavelength end of the spectrum, there is a strong decay in the photocurrent signal, presumably because there are no more QDot levels at smaller energy separation as previously mentioned. This decay seems to get steeper with increasing voltage, but in reality the ratio of signal intensity to decay is the same for all curves, which means that the effect is voltage independent, proving the point that there are no more levels available to excitation below that point. The signal intensities at the high wavelength end of the spectrum are hardly any higher than in the 870-900nm range where only thermal excitation is observed and decay to that value at a wavelength of 1300nm. The most interesting feature that appears in the spectra recorded with the white laser and consequently with a much better wavelength resolution is the multiple splitting of the wetting layer peak, which will be dealt with in more detail later.

3.4.4 Test for spatial resolution

As our first test to confine Qdots and test the spatial resolution of our PCAFM method failed, another approach was tested, namely measuring the PC at the edge of the sample. Getting close to the WL, a large increase in

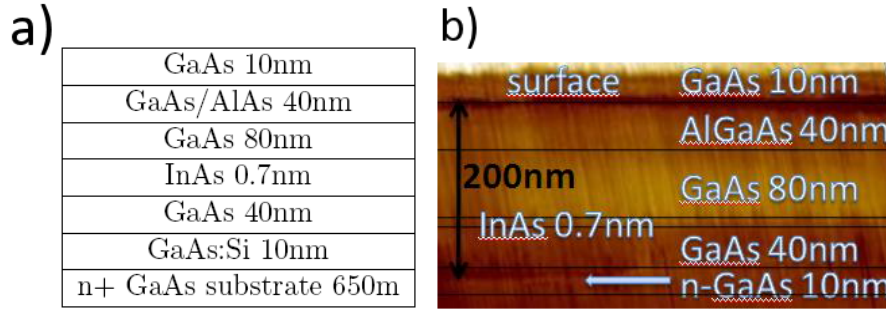


Figure 3.16: a) layer sequence of the sample. b) Photocurrent image of the sample edge showing the layer sequence.

the PC was expected and from comparing the width of the high PC band with the real width of the WL, we hoped to find the resolution of the method. Fig 3.16 shows the PC images of the sample edge and the schematic sample structure.

Comparing the sample structure with the PC image we have measured, it seems likely that the broad lighter ribbon in the image is the intrinsic GaAs region, $40+80=120\text{nm}$. The InAs layer in between could be a very slight darker line in that ribbon. Left to the ribbon, going towards the substrate, there is the highly Si doped n-GaAs region, which appears as a dark line, because the lifetime of photogenerated carriers in that area is shorter. The bright line next to it just results from surface treatment of the material before MBE deposition. Right to the ribbon, there is another bright area, presumably because of a stop in the growth process, when the surface properties can change. The thinner dark ribbon can be attributed to the AlGaAs layer. Here, the PC grows exponentially with applied bias, and at low biases, the PC intensity is lower than in GaAs. Behind that layer on the very top of the sample there should be a thin layer of GaAs, which we cannot resolve since the tip is already slipping from the sample and touching the sample edge with the side, which again gives higher PC due to the larger contact area, better contact.

3.4.5 Signal stability

Temperature stability is extremely important for the measurements. After mounting the sample, the setup needs to reach its temperature equilibrium at 35 anew. Every component needs to equilibrate so that the tip does not drift around on the sample causing a lot of noise and changing signal intensities. For our system, equilibration with respect to temperature takes about 3 hours after loading the sample. Another factor that influences signal stability is the tip-sample contact. At the start of the measurements, the tip-sample contact is generally not yet in equilibrium, as can be seen from Fig3.17 a). For the first 15minutes, first 3 curves, the signal intensity is increasing. After that time, if the tip has not been moved from the position of contact, the contact stabilises and the signal intensity remains stable for the rest of the measurement (Fig3.17 b). However if the tip is moved after recording a spectrum to a new position, different signal intensities result even after longer waiting times, as shown in Fig3.17 c). In order to obtain reproducible results, it seems to be important to let the tip-sample contact equilibrate. Fluctuations in the signal intensity are correlated with the wavelength steps $\Delta\lambda$ of the spectrum.

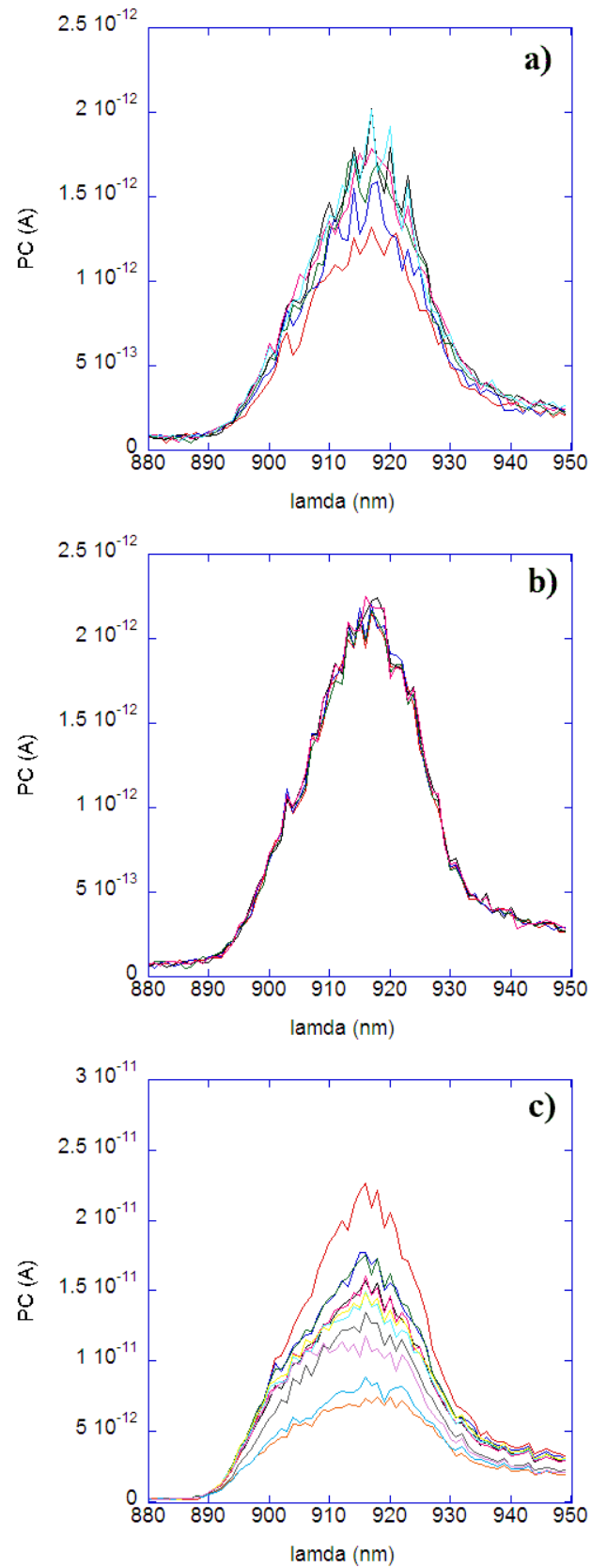


Figure 3.17: a) change of the signal intensity with time. b) stable signal after 15min c) change of signal intensity after changing position of measurement.

Chapter 4

Results

In this chapter, the results of the PC measurements are presented. First, our best spectrum showing quantum dot energy levels is presented. Then, some interesting findings about the photocurrent response of the InAs wetting layer are shown, the effects of focused ion beam (FIB) surface contamination on the photocurrent are explained and the photoresponse of samples with an aluminium oxide surface layer is investigated. Finally, spatially resolved spectra are compared to device spectra and PL spectra.

4.1 Quantum Dot Spectra

Despite the shortcomings of the halogen lamp, we did also obtain reasonably good QD spectra using it as a light source. Fig.4.1 shows three PC spectra that were recorded one after another. The first spectrum (1) shows some prominent features that correspond to dot levels at the energies 1.076eV, 1.136eV, 1.23eV, and 1.33eV. This is very similar to the data measured by [2]. Although single dot levels are supposed to be delta-function-like, a peak width in the range of the spectral resolution -30nm- can be expected and is indeed observed. In the second spectrum (2), the features are not so prominent. This is due to tip drift, because as the tip moves away from the quantum dot, the current signal in the collection region should weaken, which is just what is observed. Two peaks are basically in the same position as before just attenuated, the third peak is barely recognisable. In the last

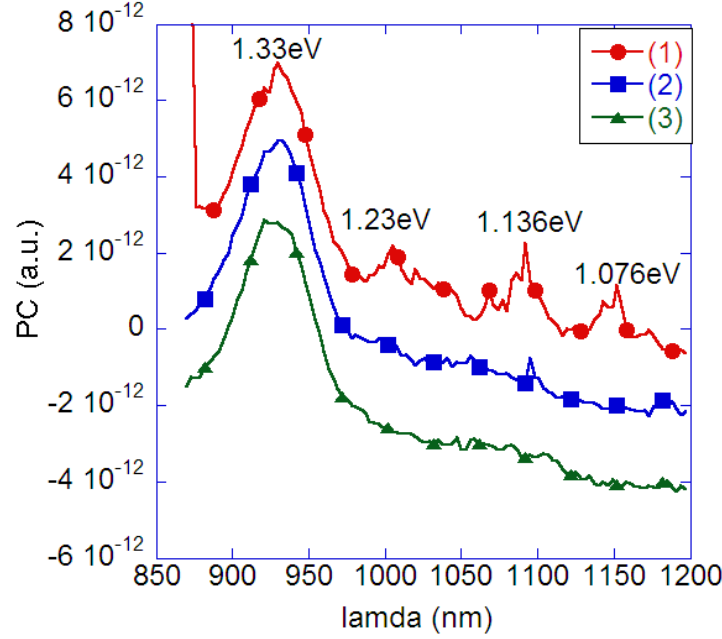


Figure 4.1: PC spectrum of an InAs quantum dot sample showing broadened quantum dot levels recorded with a halogen lamp as light source.

spectrum (3) the tip has already moved away from the quantum dot, which is not in the collection region of the tip any more and so no dot levels can be observed. Another feature of the first spectrum is a split peak for the wetting layer, which will be explained in the next section.

4.2 Splitting of the WL signal

Multiple splitting of the wetting layer peak can be nicely observed in Fig 4.2 a), measured by the PC-AFM setup. Fig 4.2 b) shows the splitting measured in a device spectrum and c) the splitting in the PL spectrum. In the PC-AFM spectrum, 4 subpeaks can be identified, the device spectrum shows three prominent peaks, where the third peak is a doublet and the PL spectrum shows a doublet. The device spectrum was recorded at 4K, the other two spectra at room temperature. The difference in spectral position of the WL peak in the PC-AFM and the device spectrum is due to the temperature difference, the energy shift follows the temperature dependence of the InAs

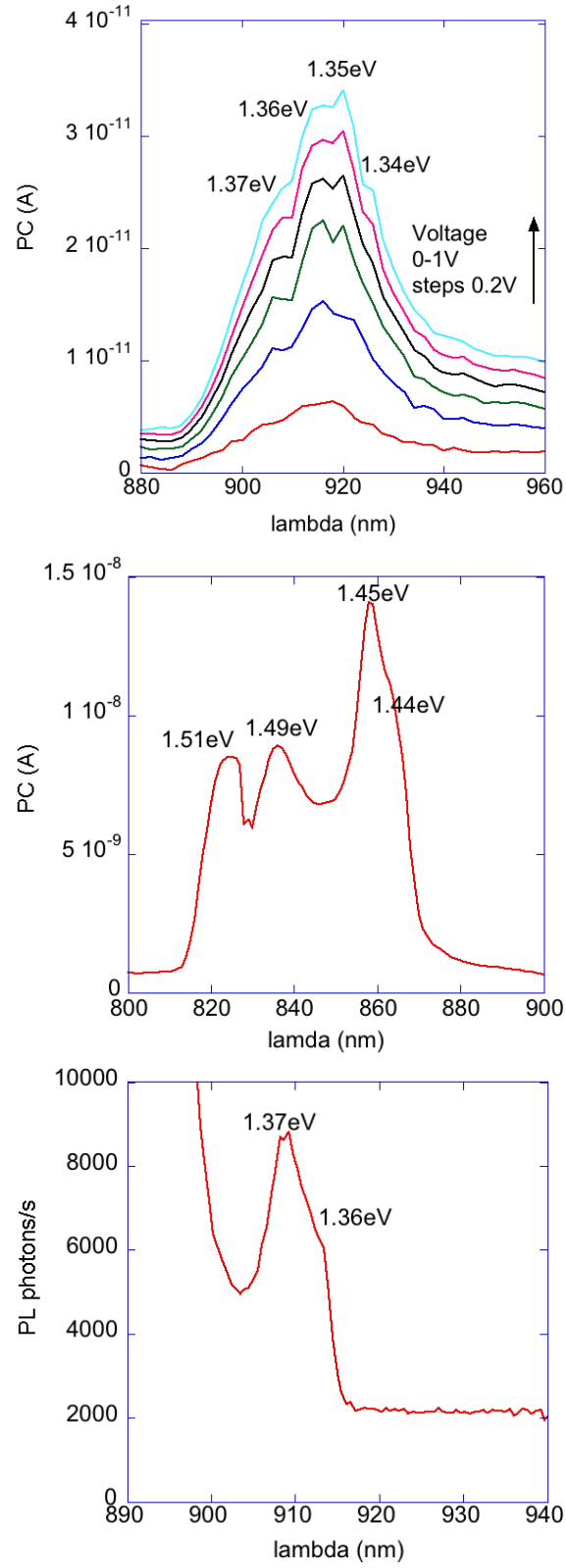


Figure 4.2: Splitting of the wettinglayer peak. From top to bottom: Bias dependent splitting recorded by pc-AFM, splitting as measured at 4K in a device configuration, double peak in the photoluminescence.

band gap energy [33] (see Fig 2.20 in Chapter 2).

There are two possible explanations for the splitting of the peaks:

- The two rightmost peaks in the AFM PC spectra at 1.35eV and 1.34eV and the double peak in the device PC spectrum at 1.45eV and 1.44eV and the PL spectrum (1.37eV, 1.36eV) are caused by spin splitting of the wetting layer peak. Rashba spin splitting exists in non-centrosymmetric materials like InAs and GaAs, under the condition that there is an asymmetric interface potential along z , which corresponds to the band bending for our samples. The splitting is linearly proportional to the electric field so the splitting is expected to increase with applied voltage. This seems to be the case, because the rightmost peaks in the voltage dependent spectrum shift slightly to the right for larger external voltages applied in the reverse direction, increasing the peak to peak separation. In case of a zero external field, when the magnitude of the E-field is given by the band bending only, the magnitude of the Rashba splitting is about 6-8meV [34], which is close to the distance of the rightmost peaks in the AFM spectra (9meV) and also to the splitting of the WL peak in the PL spectrum (8meV). The two leftmost peaks in the device spectrum (1.51eV, 1.49eV) and in the PC-AFM spectra (1.37eV, 1.36eV) could represent defect levels that are close in energy to the bandgap radiation of GaAs and couple to WL levels. These levels are most prominent in the device spectrum recorded at low temperatures.
- Another theory explaining the multiple peaks in the WL signal might be that there are several localised excitonic levels contributing to the WL peaks. The local thickness variations of the wetting layer could also shift the position of the peak by a few nm, and overlapping contributions could also explain the splitting in the ensemble spectrum.

Nevertheless, one needs to be careful not to over-interpret the PC spectra, since fluctuations and averaging routines for PC-AFM measurements can also cause small artefacts. However, there is clearly a splitting around WL energies in the AFM PC-, the device PC- and the PL data. Whether this

splitting is due to the Rashba spin splitting or a WL thickness variation is open to future investigations.

4.3 FIB effects

Our idea was to test the spatial resolution of our setup by approaching a trench cut into the sample by focused ion beam. The trench was deep enough to cut through the wetting layer, so it was assumed that no carriers would be excited in that region. In consequence, it was expected that the intensity of the wetting layer peak in the photocurrent spectrum would go down. This method was also thought to be useful to cut off individual quantum dots from the ensemble in order to obtain spectra from a few dots and possibly even from a single dot.

Unfortunately, FIB not only cuts the sample, but also implants and deposits Ga⁺ ions into the material and on the surface. The effect of the surface contamination by Ga⁺ ions on the photocurrent can be seen from the PC image in Fig 4.3 a). The PC image was recorded in the conducting mode of the AFM, the sample was illuminated using the white laser as light source from behind. The force setpoint for the AFM was 1V, and no external bias was applied. Based on the images, the following observations can be made:

- The trench areas, where the WL has been destroyed, show a high PC response, due to some Ga⁺ contamination of the surface. The PC spectrum in a trench shows no WL peak as shown in Fig4.4.
- The vicinity of the trenches is very bright due to the enhanced photocurrent from the metallised surface. The width of the bright region around the FIB structure is up to 15 μ m, so the surface is contaminated in a very broad region around the FIB trenches.
- An area that was already scanned once before the PC image in Fig 4.3 was recorded, marked as a dark square in the picture, shows reduced PC intensities. It seems that the top layer with altered properties can be removed by the mechanical impact of the tip.

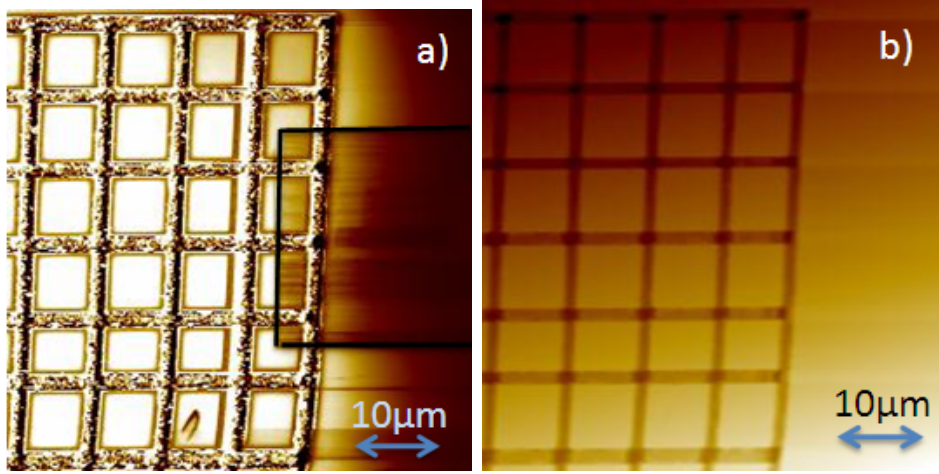


Figure 4.3: a) Photocurrent map of the FIB trenches. b) Topographic image of the same area.

The altered surface properties entail that any PC results obtained are no longer comparable to results from the plain sample surface. On the one hand, this metallic layer leads to much larger collection areas for the photocurrent, resulting in enhanced signal, as shown in Fig 4.4. On the other hand, another, much more surprising effect shows up, which is a shift of the complete spectrum towards negative photocurrent values for spectra recorded using the halogen lamp.

There are several possible explanations for this negative background, and are discussed below.

- The most likely explanation for the negative background is that the barrier that the electrons encounter at the surface appears thinner due to the destructive and metallising impact of the Ga⁺ ion beam and thus electrons are capable to escape the surface resulting in an additional electron flow that goes in the “wrong” direction. (more precisely: heavy doping with Ga⁺ can result in a very thin depletion width causing nearly Ohmic behaviour of the contact).
- Enhanced recombination of electron-hole pairs in the scattering centres introduced by the FIB treatment is also a possibility. The photogenerated electrons could be captured preferentially at the created defects

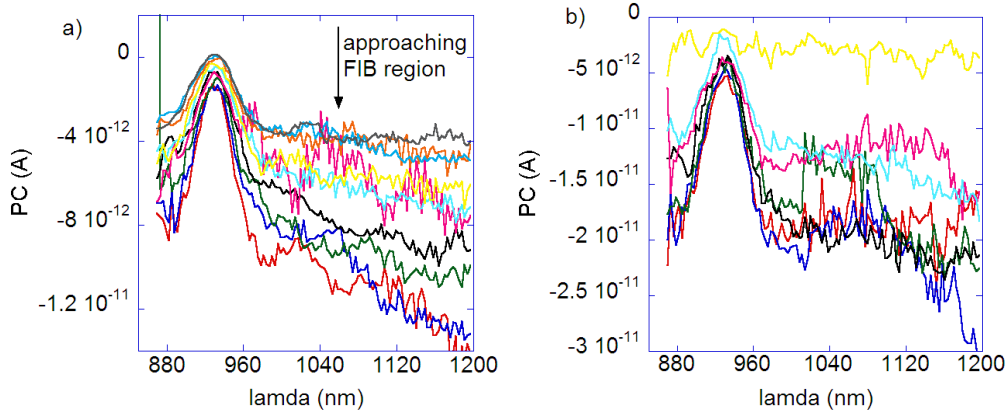


Figure 4.4: Photocurrent spectra recorded at zero bias as the tip was positioned closer and closer to the edge of the outermost FIB trench in steps of $1\mu\text{m}$. Left: distance from the trench $10\text{-}20\mu\text{m}$. Right: distance from the trench $3\text{-}9\mu\text{m}$. A halogen lamp was used as lightsource.

and not contribute to the total current, so the hole current would be larger resulting in a negative PC signal.

- The electrons coming from electron hole pairs generated in defect states near the top of the barrier could also tunnel in the wrong direction, thereby causing an additional negative background.

The shift towards negative values is much less pronounced in spectra recorded using the white laser (Fig 4.5). Here, after an initial descent of the photocurrent at values below the wetting layer, the PC recovers again. This is presumably due to the fact that the laser has a higher power and therefore generates many more holes than the halogen lamp, so that the hole current outweighs the negative background. Very high photocurrents, up to 6nA can be collected on the metallised area at 1062nm , which corresponds to the highest laser intensity output. The plateau of the curves at 1.6nA shown is a measurement artefact, since at that current value the amplifier used has reached saturation. After the seed laser peak at 1062nm in the spectrum, the measured PC intensity decays again and this decay is independent from the voltage applied to the sample. There are also several small features above 1100nm , which may come from excitation of quantum dots.

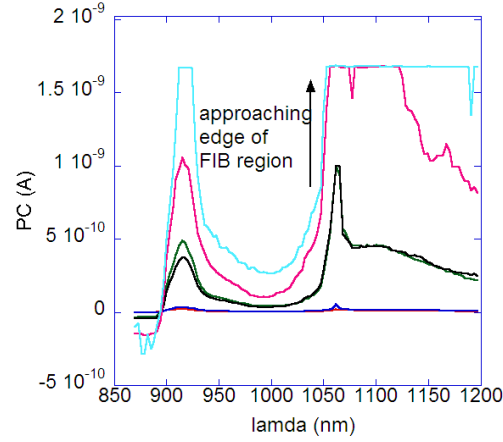


Figure 4.5: Photocurrent spectra as the tip approaches the outermost trench. The white laser served as light source.

The decay in intensity of the PC spectra in Fig4.5 at higher wavelength can be explained in the following way:

- At high wavelength (low energy) we can assume that only QDs with the lowest levels can be excited. This means that there are fewer dots with levels in that energy range and also that electrons have a larger distance to tunnel through before they can be collected. Below a certain energy, there are no more QDs with such a low energy separation, no electrons can be excited and thus no photocurrent response can be measured.

4.4 Effect of tunnel oxide on PC

Depositing a thin layer of lattice matched aluminium oxide by atomic layer deposition (ALD) can have a beneficial effect on the signal intensity. In a previous study [35] on GaAs/AlAs heterostructures it was found that at higher external bias, samples with tunnel oxide deliver higher photocurrents. This is because aluminium oxide deposited by ALD saturates dangling bonds on the sample, reducing active surface sites and thereby also reducing the band bending at the surface. Such a structure works essentially like a metal-oxide-semiconductor MOS system. The PC is measured using a soft conductive cantilever with spring constant 2.8N/m (pressures around 200MPa) that does

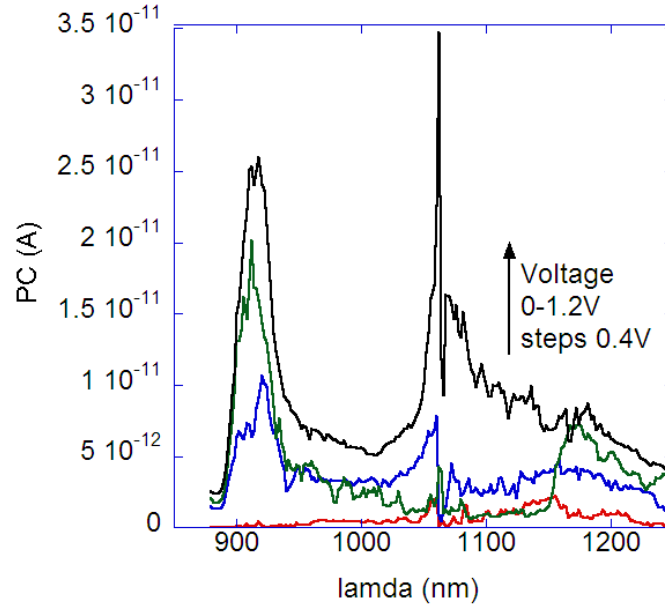


Figure 4.6: Voltage dependency of photocurrent spectra on a MOS structure with 1nm Al_2O_3 .

not scratch the oxide. Fig 4.6 shows voltage dependent spectra for a H269 sample coated with 1nm Al_2O_3 . It takes a relatively large reverse voltage of 1.2V for the signal to show the expected features and for the measurement to be repeatable.

- At zero applied voltage, the PC signal is small and unstable as shown in Fig 4.6. The reason for this is that at zero external bias, there is only a very low band bending at the surface. Therefore only very few charge carriers manage to escape the InAs quantum well through thermal excitation and only diffusion currents contribute to the signal.
- With increasing reverse bias (+V sample bias), the wetting layer peak starts to appear and at 1.2V the spectrum shows similar features as the samples without ALD oxide. The signal intensity is high, but the features are not as smooth as in spectra without oxide. There is a drop in PC intensity just after the seed laser peak, possibly due to the quickly changing charge carrier concentration at the oxide layer.

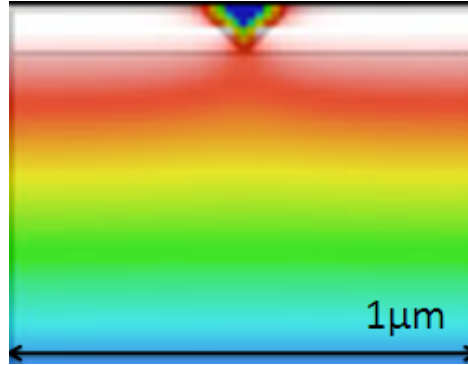


Figure 4.7: Potential distribution under an AFM tip assuming a MOS-type junction. Adapted from [27].

- The spectrum appears at increasing reverse bias, because the electric field and band bending increase in the vicinity of the tip, in the near surface region. The situation corresponds to the n-MOS depletion case, where the positive gate bias pushes electrons away from the oxide layer, which subsequently leads to an increase in the depletion layer width.
- Since there are no bound surface states to neutralise the holes, the extension of the space charge zone in horizontal direction is larger than in case of the Schottky contact. As it can be seen from Fig. 4.7, the potential distribution is wider [27], which leads to an increased collection area, and consequently also results in enhanced PC signal intensities and reduced spatial resolution.
- Through photogeneration, additional charge carriers are produced. Holes drift in the field of the depletion region towards the tip and electrons towards the back contact. The hole concentration at the oxide layer is determined by the balance between photogeneration rate and tunneling rate through the oxide. The capacitance of the depletion region decreases, the voltage drop across the oxide increases with increasing light intensity. The tunneling rate is determined by the voltage across the oxide. [36, 25] At moderate bias, the photocurrent is proportional to the intensity of incident light.

- A possible reason for the signal drop just behind the wetting layer could be that under strong illumination, many charge carriers are created and this changes the electric field in the depletion zone. This variation in the electric field could cause a variation in the PC response.

Data quality is not any better than in case of samples without the ALD oxide, presumably due to the large collection region and the changing capacitance of the depletion layer.

4.5 Comparison of PC-AFM and device PC spectra

Fig4.8 a) shows the device spectrum of a H269 sample at 4K as compared to the PCAFM spectrum at RT in b). Both spectra clearly show the WL peak and the seed laser peak. The kink in the PCAFM spectrum at 1170nm in all spectra is an artefact from the laser, the PC follows the change in laser output intensity. Although barely visible, this also happens in the device spectrum. The WL peak is split 4-fold in the device spectrum, and at least 2-fold in the PCAFM spectrum. A pronounced WL peak dominates the device spectrum while the seed laser peak is not so strong and the PC spectrum shows the opposite behaviour. The device had macroscopic contacts and was illuminated without focusing or dispersing optics thorough the glass fiber with 200 μ m diameter. For the PCAFM spectrum spectrum a conducting AFM tip was used.

- The WL peaks in Fig. 4.8 a) and b) appear at different wavelength position due to the temperature dependent shift in bandgap energies. For the device spectrum recorded at 4K there is a shift of about 70nm towards lower wavelength as compared to the RT PCAFM spectrum, which corresponds to the decrease of the InAs bandgap in this temperature range [33].
- The higher intensity of the seed laser peak in the PCAFM spectrum is probably due to the fact that the broadband laser influences the AFM

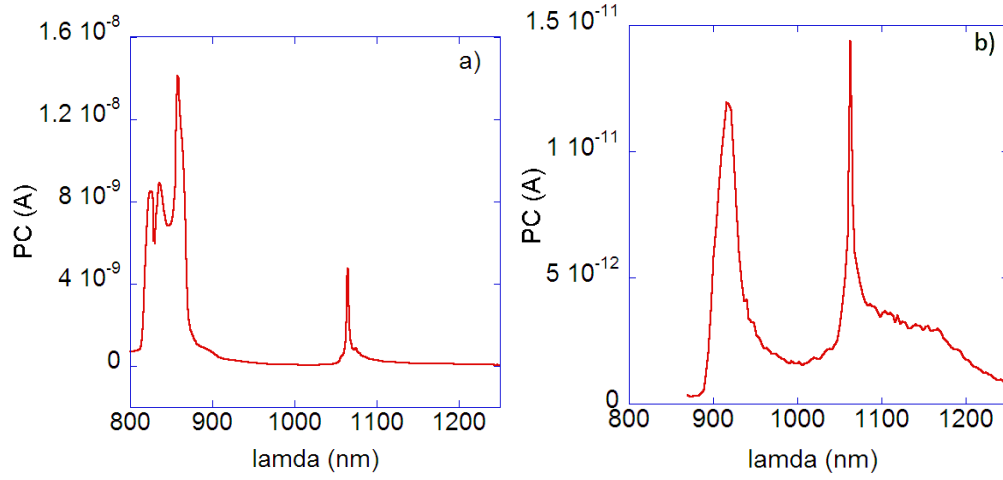


Figure 4.8: a) Device spectrum. b) PC-AFM spectrum.

feedback at very high intensities around the seed wavelength, which can be seen from the error signal of the instrument. This could result in increased pressure to the surface, yielding higher PC intensities due to better contact.

- The difference in intensities of the WL peaks in the two spectra is a result of the different sizes of the current collection regions. The device uses the photogenerated carriers from the complete illuminated area with diameter of about $200\mu\text{m}$. The collection region of the AFM tip has a diameter of about 200nm , as discussed in Chapter 2. So it can be expected that the WL peak is more intense in the device spectrum, since more charge carriers from larger area can contribute to the current.

4.6 Comparison of PC and PL results

PL spectra were also recorded of the H269 samples (Fig 4.9 a)) using confocal photoluminescence. The strong increase in luminescence around 880nm is due to excitation across the GaAs bandgap. The wetting layer signal is a double peak at 908nm and 913nm , which is shifted by only 6nm compared to the two main peaks in the PC spectrum, which are at 914nm and 921nm . The PL spectrum is then flat up to 1155nm , where there are several repeating

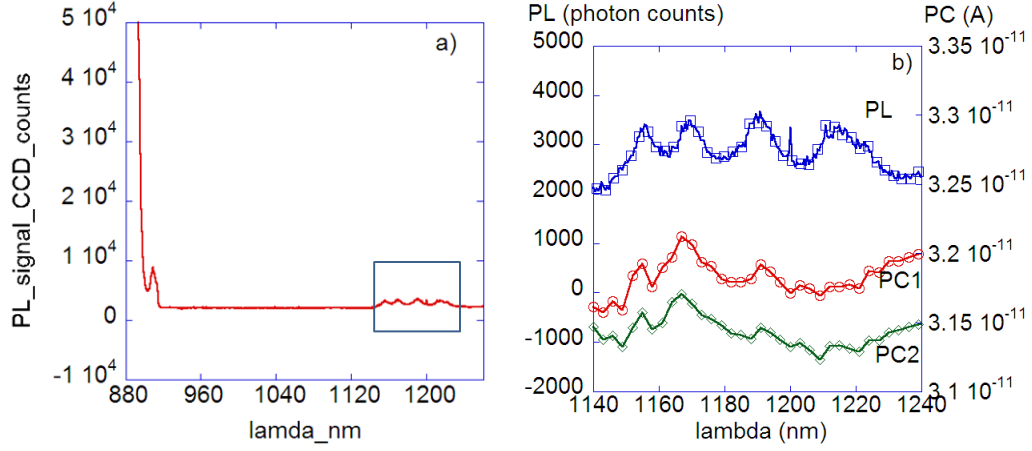


Figure 4.9: a) Micro-photoluminescence of H269. b) Comparison of PL and PC signals.

peaks, with peak-to-peak distance in the order of the InAs phonon energy, around 20-25 meV. On a closer look, these peaks also correlate with peaks in the PC spectra, as shown in Fig 4.9 b). There is a one-to one correspondence of the first three peaks, but the 4th peak is only present in the PL spectrum. This shows that transitions can be observed by both absorption and emission techniques but certain transitions involving electron-phonon interactions are better observed by PL. The 4th peak is probably a phonon replica of the previous peaks. Measurements showed that these signals are also present in PL spectra of plain GaAs, but have different intensities depending on the doping level of the GaAs substrate. It is most likely that these levels show the photoresponse of trap levels in GaAs, and the signals are due to pair recombination in such defects.[37, 38].

Chapter 5

Conclusion and Outlook

Photocurrent AFM spectroscopy is a powerful tool to probe the photore-sponse of the sample locally. It was shown that the high output intensity of the broadband laser excitation source leads to enhanced PC signals in-tensities and allows for better spectral resolution, since a smaller band of a spectrum can be selected. In addition, measurement times could be reduced as a result of the strong, reliable photocurrent signal. Care has to be taken to keep the temperature and the pressure constant in order to have repro-ducible measurements. The sub-100nm spatial resolution of the instrument is a blessing and a curse. On the one hand, the PC-AFM is capable to record spectra of an individual QD, on the other hand, locating burried dots is on samples with low dot density proved to be very difficult. Higher dot den-sity would increase the probability of finding a dot with the tip, but also the probability that the signal does not only come from a single dot but an ensemble. The attempt to localise dots by fabricating a grid structure using FIB failed due to the strong surface contamination deposited by the FIB beam. Further tests should be made to determine the exact detector volume at different doping levels and a method for localising burried dots needs to be found. The good spectral resolution of the instrument allows for accurate determination of the position of excited levels, and allowed for the observa-tion of a splitting of the InAs wetting layer peak. The instrument is also sensitive to weak transitions from defect levels, where the intensity depends on the density of impurity states. In order to make the interpretation of

the spectra easier, filtering of the seed laser wavelength would be beneficial. The seed laser wavelength at 1062nm happens to be in the range where QD levels are expected, so removing only a bandwidth of about 5-10nm around the peak would be useful.

The PC-AFM provides a complementary method to PL to investigate electronic transitions in semiconducting samples. It could be routinely used to test the energy levels of QDs for lasing and IR applications, to test the local photoresponse of nanostructured solar cells, map the percolation current pathway in conducting nanoparticle films, test the photogeneration of organic films. By increasing the measurement speed and accuracy, scanning PC spectroscopy might become possible, where a full spectrum at every measurement point of the photocurrent map can be obtained.

Acknowledgements

I would like to thank

- Prof. Jürgen Smoliner for making this work possible, for his help with setting up the new optics and especially for his support with discussions and readiness to help to clarify my many questions.
- Dr Wolfgang Brezna for introducing me to the setup, for many discussions and for helping out with every problem I had. I especially thank him for his patience and advice related to composing this document.
- DI Roman Bruck, BSc Jonathan Silvano de Sousa, DI Peter Rödinger and DI Christian Eckhardt for their help with LaTeX and discussions and all the other staff of the FKE for the good working atmosphere.
- My parents for their supportive attitude in times of stress.

Bibliography

- [1] I.E.Itskevich et.al P.W.Fry, D.J.Mowbray. Photocurrent Spectroscopy of InAs/GaAs Self-Assembled Quantum Dots. *Phys. stat. sol. b*, 224:497, 2001.
- [2] S.R.Parnell et.al. P.W.Fry, I.E.Itskevich. Photocurrent spectroscopy of InAs/GaAs self-assembled quantum dots. *Physical Review B*, 62:16784, 2000.
- [3] J.M.Calleja J.M.Becker R.J.Haug K.Pierz D.Sarkar, H.P.van der Meulen. Phonons in InAs/AlAs single quantum dots observed by optical emission. *Phys.Rev. B*, 71:081302(R), 2005.
- [4] H.Nakamura K.Tanaka, N.Kotera. *J. Appl. Phys.*, 85:4071, 1999.
- [5] K.Ploog R.T.Collins, K.v.Klitzing. Photocurrent spectroscopy of GaAs/Al(x)xGa(1-x)As quantum wells in an electric field. *Phys.Rev. B*, 33:4378, 1986.
- [6] B.Xu P.Jin Ch.Zhao L.K.Yu Z.G.Wang W.Lei, Y.H.Chen. Interband and intraband photocurrent of self-assembled InAs/InAlAs/InP nanostructures. *Nanotechnology*, 16:2785, 2005.
- [7] W.Brezna J.Smoliner G.Strasser K.Unterrainer G.Fasching, F.F.Schrey. Photocurrent spectroscopy of single InAs/GaAs quantum dots. *Phys. Status Solidi C*, 2:3114, 2005.
- [8] Ch.Lienau J.Luft A.Richter, J.W.Tomm. Optical near-field photocurrent spectroscopy: A new technique for analyzing microscopic aging processes in optoelectronic devices. *Appl. Phys. Lett.*, 69:3981, 1996.

-
- [9] K.Unterrainer G.Strasser J.Smoliner W.Brezna, G.Fasching. Atomic force microscopy based room temperature photocurrent-spectroscopy of single subsurface InAs quantum dots. *physica status solidi C*, 1:1–4, 2009.
- [10] T.Roch A.M.Andrews W.Brezna J.Smoliner G.Strasser K.Unterrainer G.Fasching, F.F.Schrey. Single InAs/GaAs quantum dots: Photocurrent and cross-sectional AFM analysis. *Physica E*, 32:183, 2006.
- [11] Ch.Gerber G.F.Binnig, C. F.Quate. Atomic Force Microscope. *Phys.Rev.Lett*, 56:930, 1986.
- [12] D.S.Ginger L.S.C.Pingree, O.G.Reid. Electrical Scanning Probe Microscopy on Active Organic Electronic Devices. *Adv. Mater.*, 21:19, 2009.
- [13] M.Takeuchi T.Takahashi H.Masuda. Local photocurrent detection on InAs wires by conductive AFM. *Ultramicroscopy*, 105:137, 2005.
- [14] K.Komori T.Amano, T.Sugaya. 1.3 micrometer InAs Quantum-Dot Laser With High Dot Density and High Uniformity. *IEEE Phot.Technol.Lett.*, 18:619, 2006.
- [15] S.C.Lee S.F.Tang, S.Y.Lin. InAs/GaAs Quantum Dot Infrared Photodetector (QDIP) With Double Al_{0.3}Ga_{0.7}As Blocking Barriers. *IEEE Transact. Elect.Dev.*, 49:1341, 2002.
- [16] D.Gammon L.J.Sham X.Li, D.Steel. Quantum information processing based on optically driven semiconductor quantum dots. *Optics & Photonics News*, page 38, 2004.
- [17] S.M.Sze. *Physics of Semiconductor Devices*. Wiley-Interscience, 1981.
- [18] T.Walther M.A.Migliorato M.Hopkinson A.G.Cullis, D.J.Norris. Stranski-Krastanow transition and epitaxial island growth. *Phys.Rev. B*, 66:081305(R), 2002.
- [19] L.Krastanow I.N.Stranski. *Sitzungsber. Akad. Wiss. Wien, Math.-Naturwiss. Kl., Abt. 2B*, 146:797, 1938.

-
- [20] Wikipedia. Schematics of light path in a Czerny-Turner monochromator.
 - [21] Newport. Diffraction Gratings Handbook.
 - [22] Wikipedia. Schematics of a Schottky junction.
 - [23] S.M.Sze A.M.Cowley. Surface States and Barrier Height of Metal-Semiconductor Systems. *J.Appl.Phys.*, 36:3212, 1965.
 - [24] S.M.Sze C.R.Crowell. Current transport in Metal-Semiconductor Barriers. *Solid-State Electronics*, 9:1035, 1966.
 - [25] W.T.Liu C.-H.Lin B.-C.Hsu, C.W.Liu. A PMOS tunneling photodetector. *IEEE Transact. Electr. Dev.*, 48:1747, 2001.
 - [26] V.L.Rideout. A Review of the Theory and Technology for Ohmic Contacts to Group III-V Compound Semiconductors. *Solid-State Electronics*, 18:541, 1975.
 - [27] O.Bethge E.Bertagnolli-J.Smoliner C. Eckhardt, W.Brezna. Tip Geometry Effects in Scanning Capacitance Microscopy on GaAs Schottky and MOS-Type Junctions. *Phys. Rev.*, *accepted for publication*, 2009.
 - [28] T.J.Drummond. Schottky barriers on GaAs: Screened pinning at defect levels. *Physical Review B*, 59:8182, 1999.
 - [29] Ioffe Physical Technical Institute of Russia.
 - [30] M.D'Amato. Schematics of an AFM.
 - [31] C.D.Frisbie T.W.Kelley, E.L.Granstrom. Conducting Probe Atomic Force Microscopy: A Characterization Tool for Molecular Electronics. *Adv. Mater.*, 11:261, 1999.
 - [32] W.Brezna J.Smoliner. An intercepted feedback mode for light sensitive spectroscopic measurements in atomic force microscopy. *Revi.Sci.Instru.*, 78:106104, 2007.

-
- [33] A.Stintz K.J.Malloy D.P.Popescu, P.G.Eliseev. Temperature dependence of the photoluminescence emission from InAs quantum dots in a strained Ga_{0.85}In_{0.15}As quantum well. *Semicond.Sci.Technol.*, 19:33, 2004.
- [34] H.Takayanagi T.Enoki J.Nitta, T.Akazaki. Gate Control of Spin-Orbit Interaction in an Inverted In_{0.53}Ga_{0.47}As/In_{0.52}Al_{0.48}As Heterostructure. *Phys.Rev.Lett*, 78:1335, 1997.
- [35] J.Smoliner W.Brezna, G.Strasser. Force- and bias-dependent contrast in atomic force microscopy based photocurrent imaging on GaAs-AlAs heterostructures. *Semiconductor Science and Technology*, 22:1209–1212, 2007.
- [36] M.H.Lee W.S.Kuo B.C.Hsu C.W.Liu, W.T.Liu. A novel photodetector using MOS tunneling structures. *IEEE Electron Device Lett.*, 21:307, 2000.
- [37] G.Burns M.I.Nathan. Recombination radiation in GaAs. *Physical Review*, 129:125, 1963.
- [38] A.E.DiGiovanni R.C.C.Leite. Frequency shift with temperature as evidence for donor-acceptor pair recombination in relatively pure GaAs. *Physical Review*, 153:153, 1967.

Project „Photocurrent measurements on InAs quantum dots“

Start date: 01.12.2008

End date: 10.05.2009

Goal: Implementation and testing of a new broadband laser as light source for photocurrent measurements by means of conducting atomic force microscopy.

Deliverables:

- Functional setup for illumination with the broadband laser
- Calibration of the instrument
- Documentation

Time schedule:

Project step	Deadline
Familiarise with the equipment	30.12.2008
Implementation of a new light source	30.01.2009
Testing parameters	30.03.2009
Photoluminescence	30.04.2009
Documentation (write-up)	10.05.2009

Costs:

Equipment operation	Estimated cost
Koheras Versa laser source	1870€
PicoPlus AFM	4200€
Keithley SMU	320€
Consumable materials	
Tips	2100€
Optical components	540€
Miscellaneous	230€
Salaries	
Supervisor	4160€
Student support	2760€
Estimated total	16.200€